Fuel 428 (2027) 140328

Contents lists available at ScienceDirect

Fuel

journal homepage: www.elsevier.com/locate/fuel

Full Length Article

Development of a phenomenological spray model for next generation dual-fuel marine engines: validation in free-field conditions

Shadab Heidarabadi [a,*], Hamidreza Maleki Almani [a,b], Alireza Kakoee [a], Amin Andwari [c], Jari Hyvönen [d], Maciej Mikulski [a,*]

[a] Efficient Powertrain Solutions (EPS), School of Technology and Innovation, University of Vaasa, Wolffintie 34, FI-65200 Vaasa, Finland
[b] Department of Mathematics and Statistics, School of Technology and Innovations, University of Vaasa, Wolffintie 34, FI-65200 Vaasa, Finland
[c] Machine and Vehicle Design (MVD), Materials and Mechanical Engineering, Faculty of Technology, University of Oulu FI-90014 Oulu, Finland
[d] Wärtsilä Finland OY, FI-65170 Vaasa, Finland

ARTICLE INFO

Keywords:
Phenomenological spray model
Fuel–air stratification
Dual-fuel marine engine
RCCI
Spray penetration

ABSTRACT

This study develops and validates a reduced-order phenomenological spray model for dual-fuel marine engines operating under reactivity controlled compression ignition (RCCI) conditions. Rather than introducing a new spray-theory class, the work adapts a Musculus-based formulation into an RCCI-oriented framework capable of predicting both spray penetration and cylinder-fixed fuel–air stratification at low computational cost. The main methodological advance is the introduction of a CV-to-zone mapping strategy for transferring spray control-volume information into the zonal structure required by multi-zone combustion models; among the three tested approaches, an angled non-uniform mapping gave the most accurate stratification representation. Validation is via high-speed optical measurements by the Optical Spray Combustion Chamber and high-fidelity CFD simulations with CONVERGE. Sensitivity analysis identified the discharge coefficient (Ca) and velocity profile factor (β) as dominant calibration parameters, with profile evolution factor (α) serving as a secondary shaper of radial distribution. A two-stage optimization strategy for local tuning per case and global tuning across conditions demonstrated that the globally calibrated model reproduces spray penetration within ~14% of CFD, and peak high-reactivity fuel location within ±2 zones across calibration and validation datasets. Amplitude prediction of peak fuel fraction exhibited larger scatter (~40%), but location fidelity was robust. The framework provides a reliable and computationally efficient surrogate for spray-mixing dynamics and is well suited for future integration with fast 0D/1D multi-zone combustion models to support predictive, cycle-resolved simulation of advanced RCCI engines.

1. Introduction

Marine transportation underpins the global economy, handling over 90% of worldwide trade [1,2]. However, it contributes approximately 3% of global greenhouse gas (GHG) emissions [3], along with a significant share of NOx/SOx (13%) and particulate matter (4%) emissions [4]. Under business-as-usual conditions, these impacts are expected to increase, with projections indicating up to a 25% rise in GHG emissions by 2050 [3,5]. Decarbonization remains challenging due to stringent power density and durability requirements, which sustain reliance on combustion engine technology and flexible adoption of zero-carbon fuels [6,7].

Recently, the marine sector has adopted reactivity controlled compression ignition (RCCI) as a development pathway for next-

Abbreviations: 0D, Zero-dimensional; MAPE, Mean absolute percentage error; 1D, One-dimensional; MH, Multi-hole; AMR, Adaptive mesh refinement; MSE, Mean squared error; CAD, Crank angle degrees; MZM, Multi zone model; CFD, Computational fluid dynamics; NOx, Nitrogen oxides; CFL, Courant-Friedrichs-Lewy; OSCC, Optical spray combustion chamber; CVs, Control volumes; RCCI, Reactivity controlled compression ignition; DOE, Design of experiments; RMSE, Root-mean-square error; EOI, End of injection; RNG, Renormalization group; EVO, Exhaust valve opening; ROSM, Reduced-order spray model; FD, Fuel distribution; RT, Rayleigh–Taylor; GHG, Greenhouse gas; LRF, Low-reactivity fuel; HRF, High-reactivity fuel; SOC, Start of combustion; HRR, Heat release rate; SOI, Start of injection; IVC, Intake valve closing; STH, Sustainable Technology Hub; KH, Kelvin–Helmholtz; TDC, Top dead center; LFO, Light fuel oil; THC, Total unburned hydrocarbons; LHS, Latin hypercube sampling; UVATZ, University of Vaasa Advanced Thermo-kinetic multizone model.

* Corresponding authors.
E-mail addresses: Shadab.heidarabadi@uwasa.fi (S. Heidarabadi), maciej.mikulski@uwasa.fi (M. Mikulski).

https://doi.org/10.1016/j.fuel.2026.140328
Received 15 January 2026; Received in revised form 13 May 2026; Accepted 8 June 2026
Available online 18 June 2026
0016-2361/© 2026 The Author(s). Published by Elsevier Ltd. This is an open access article under the CC BY license (http://creativecommons.org/licenses/by/4.0/).

generation fuel-flexible engines [8]. This progress combines experimental engine studies, model-based development approaches [9,10], and the design of advanced control strategies for robust and efficient operation [11,12]. A notable milestone is the Wärtsilä RCCI pilot [13], which has progressed to sea trials onboard M/V Aurora Botnia, operated by Wasaline. Reported results demonstrate 90% reduction in NOx emissions, approaching automotive Euro VI levels, along with a ~50% reduction in methane compared to best-in-class dual-fuel engines. A comprehensive overview of RCCI development for marine applications is provided by Mikulski et al. [14].

Relying on in-cylinder blending of fuels with different reactivity [15], RCCI is inherently fuel-flexible [16]. Typically, a low-reactivity fuel (LRF), such as methanol [17,18], natural gas [19], or ammonia [20,21], is premixed with air, while a small amount of high-reactivity fuel (HRF) is directly injected very early during the compression stroke [22]. This creates a controlled in-cylinder fuel-reactivity stratification, which governs autoignition, followed by almost volumetric (very efficient), locally and globally lean combustion, which avoids high-temperature/low oxygen content emission formation regions [23,24].

Despite its potential, RCCI faces challenges. These include high hydrocarbon emissions at partial loads [25], combustion harshness and thermal loading at high loads [26], and limited controllability during transient and cycle-to-cycle operation [27]. Addressing these issues is inherently complex, as RCCI performance depends on a large calibration space, particularly when advanced control actuators such as sequential injection and variable valve actuation (VVA) [28,29] are employed. This renders conventional experimental approaches insufficient and necessitates predictive computational models capable of supporting large-scale co-optimization campaigns [30].

As reactivity stratification is the governing control mechanism in RCCI, modeling of spray–combustion interaction is essential. To support model-based calibration and control design, the simulation approach must be both predictive and computationally efficient, a significant challenge given the phenomenological complexity of spray formation and its coupling with thermo-kinetic processes in the cylinder [31].

The contemporary approaches for control-oriented modeling of RCCI involve multi-zone models (MZMs) that solve reaction kinetics (as the dominant combustion mechanism) across the zero-dimensional reactor network. Other processes, like interzonal mass and heat transfer or spray formation, are typically modeled phenomenologically or semi-empirically [31]. Most common approaches for capturing the effect of spray-induced fuel distribution rely on an imposed profile, either directly from CFD results [30], or indirectly as a generic shape – tunable along with the whole combustion model, directly to engine test results [32,33]. These approaches are fast but in general non-predictive; requiring intensive pre-processing (computationally heavy CFD) or a large amount of experimental tests to develop an in-principle case-dependent model calibration.

Reduced-order phenomenological spray models have emerged as a promising response to this dilemma, offering a good balance between predictive capability and computational cost [34]. Within this class, 0-D and 1-D models are designed to predict the macroscopic spray features with minimal computational expense. They typically rely on turbulent-jet self-similarity, simplified momentum-based analysis, and empirical correlations. Classical examples include the models of Wakuri et al. [35], Hiroyasu and Arai et al. [36], and Siebers et al. [37], which provide compact algebraic descriptions of spray penetration. More recent developments have extended these formulations to modern injection systems. Desantes et al. [38] emphasized the role of injection momentum flux, particularly during the early stage of injection. Kostas et al. [39] reported a $t^{3/2}$ scaling during the initial penetration stage, Zhou et al. [40] proposed a five-stage formulation for improved fitting accuracy, and Zhai et al. [41,42] developed a two-stage model for micro-hole nozzles under ultra-high injection pressure.

Despite their efficiency, quasi-steady formulations are not sufficient for transient injection events [43], especially during the initial injection period and after the end of injection (EOI). After EOI, the problem becomes more complex because spray mass and momentum both vary with time, rendering steady control-volume assumptions inadequate. To address this, Pastor et al. [44] introduced a transient axial discretization framework, and Musculus et al. [45] proposed a 1-D discrete model that captured the enhanced near-nozzle entrainment after EOI, known as the entrainment wave. Although these approaches provide important physical insight, they remain too computationally demanding for real-time optimization or repeated control-oriented simulations. Simpler reduced-order post-EOI models were therefore proposed by Liu et al. [46] and supported experimentally by Bao et al. [47], showing that, sufficiently far after EOI, spray tip penetration approaches a fourth-root dependence on time. More recently, Kurapati et al. [48] developed the 1D SprayLet approach, a cross-sectionally averaged gas–liquid spray model coupled to CFD through conservative mass, momentum, and heat-transfer source terms. The model was introduced to reduce grid dependence in commonly used droplet-based spray models and improve statistical convergence.

Nevertheless, existing reduced-order spray formulations still have an important limitation in the RCCI context. Most models predict only spray penetration, while spatial fuel distribution is usually treated as a combustion-model-specific feature rather than a standalone predictive capability of the spray model. Yet, for RCCI combustion, the latter is essential because the local distribution of high-reactivity fuel governs mixture stratification and therefore strongly affects ignition, heat release, and emissions.

Only a limited number of studies have addressed spray-resolved fuel stratification for early-injection RCCI, particularly considering specific features of marine engines. De Bellis et al. [32] represented an important step toward physics-based multi-zone modeling; however, the spray treatment remained fundamentally imposed rather than predictive. In that framework, the in-cylinder LFO distribution was prescribed through an exponential surrogate controlled by a tuning parameter σ, with stratification restricted to axisymmetric radial gradients and without interzonal mass transfer. As a result, the approach retained the computational efficiency of a reduced-order formulation, but not the predictive flexibility required to respond physically to changes in injection settings, engine geometry, or operating conditions.

By contrast, De Felice et al. [49] advanced the framework by integrating a control-volume spray-jet model and validating spray penetration against constant-volume chamber experiments, including post-EOI entrainment-wave effects. More recently, the same group extended this spray-informed strategy to ammonia–diesel RCCI within a broader phenomenological framework that also includes evaporation, interzonal diffusion, ignition, flame propagation, and pollutant-emission sub-models [33].

Taken together, these studies represent a major step towards spray-informed RCCI multi-zone modeling. However, a key issue remains: in both frameworks, the predictive capability of the spray treatment is validated mainly through spray penetration and agreement of the fully coupled combustion model with engine-level observables (pressure, heat release, performance, emissions), rather than through independent validation of in-cylinder fuel stratification. As a result, although these studies demonstrate the relevance of spray-resolved stratification for RCCI combustion modeling, they do not yet establish the spray formulation as an independently assessable, reduced-order surrogate whose predictive capability is demonstrated not only for spray penetration, but also for cylinder-fixed zonal fuel-distribution evolution under early-injection marine RCCI conditions. In that sense, the approaches create an immense problem for model calibration as both combustion and spray phenomena cannot be calibrated and validated sequentially, resulting in an immense number of tuning parameter combinations. Handling this complexity problem in a real calibration endeavor requires a set of governing assumptions that fix certain model parameters, effectively sacrificing model generalizability to different engine

platforms or fuels.

In the present study, this critical gap in RCCI-oriented reduced-order modeling is addressed by developing and validating a physics-based phenomenological spray surrogate for early-injection marine dual-fuel engines. The work adapts a Musculus-based formulation to RCCI-relevant conditions and extends it toward direct prediction of both spray penetration and cylinder fuel stratification. The model is designed to generate spray/stratification inputs for reduced-order RCCI multi-zone combustion modeling. Particular emphasis is placed on the modular coupling between the spray control volume and the combustion zones through three CV-to-zone mapping strategies, whose performance is systematically assessed through high-fidelity CFD simulations.

The study proves that the momentum-flux-related parameters Ca and β primarily govern the stratification response calibration, highlighting injection-momentum scaling as a physically meaningful and generalizable principle for spray-driven combustion modeling in RCCI engines. The physics-based structure of the model requires only limited CFD data for model pre-calibration, and enables that spray model calibrated on one selected geometry can capture differences across the studied injection and operating conditions. This makes the approach well-suited for combustor-injector interaction-driven control parameter optimizations when coupled with contemporary MZM frameworks. In that sense, the approach excels over legacy RCCI modeling approaches which locked this possibility only for pre-defined injection patterns.

2. Methodology

2.1. Experimental setup and reference data

This study benchmarks the simulations against experiments conducted in the Optical Spray Combustion Chamber (OSCC) at Wärtsilä's Sustainable Technology Hub (STH), Vaasa, Finland [50]. The OSCC is a constant-volume chamber with a large test volume and minimal obstructions, providing clear optical access and reproducible pre-injection thermodynamic conditions. These features make it well-suited for spray visualization [51]. The chamber is designed for evaluating fuel injection systems used in large marine engines, following the principles described by Baert et al. [52]. It can be operated either in cold conditions combined with non-reactive conditions, or in hot conditions with either reactive or non-reactive conditions. When operating the chamber in hot, non-reactive conditions, the gas mixture for the pre-combustion is calculated so that all oxygen is consumed during the pre-combustion event. This leaves the chamber with pressure and temperature similar to an internal combustion engine, but with no oxygen present. Table 1 summarizes its features. The chamber is cubical and fitted with a gas exchange system, an injector adapter, and optical windows. Spray visualization is possible through any of the four windows, depending on the test setup. Hydraulic gas exchange valves, exhaust pipes, and gas lines are located at the back of the chamber. To ensure consistent test conditions, the chamber was emptied and refilled using the exhaust and inlet valves after every five sprays. This procedure minimized the risk of fuel mist affecting the primary spray structure [50].

The diesel injector was mounted upside down inside the chamber body. This marine diesel injector features a nine-hole nozzle, with parameters listed in Table 2.

Table 1
Key specifications of the Optical Spray Combustion Chamber (OSCC).

Parameter	Value
Outer dimensions	600 × 600 × 550 mm
Volume	0.0172 m^3 (17.2 l)
Pressure	0–400 bar
Temperature	20–200 °C
Operation modes (Cold)	Non-reactive sprays
Operation modes (Hot)	Reactive or non-reactive sprays
Heat and pressure generation (Cold)	Pressurized air
Heat and pressure generation (Hot)	Pre-combustion

The nozzle holes have a K-factor of zero, meaning the holes are cylindrical (parallel walls), so the inlet and outlet diameters are equal. Throughout testing, the injector was maintained at 300 K to ensure temperature stability, as all laboratory tests were performed at room temperature. The test campaign utilized natural gas with a methane number of about 80 as LRF, and light fuel oil (LFO) as HRF. This commercial LFO had a density of 833.5 kg/m^3 at 15 °C and a kinematic viscosity of 3.036 mm^2/s at 40 °C. A common-rail injector was used for LFO injection. Furthermore, this injection featured early timings and quick durations, suggesting an RCCI operation. Table 3 shows the LFO properties.

2.2. CFD model setup

CFD simulations were performed with CONVERGE Studio 3.1 to model non-reactive spray evolution, while an auxiliary reactive closed-cycle CFD setup was used later for combustion-oriented validation. The CFD setup and sub-model selections used in this study follow a previously validated CONVERGE framework developed for the same marine RCCI engine platform [9]. A compact summary of the adopted modeling assumptions is provided in Table 4, while the detailed rationale behind the selection is provided in Appendix D.

The setup represents the injector-chamber interaction under RCCI-relevant conditions, from intake valve closing (IVC) through exhaust valve opening (EVO). At IVC, the cylinder charge consisted of air with a homogeneously premixed CH_4/C_2H_6 blend, while diesel fuel was represented by n-dodecane ($C_{12}H_{26}$) for both mixing and spray behavior. This CFD simulation used a modified KH-RT model for spray breakup (no preset breakup length) [53]. Droplet evaporation followed the Frössling method [54]. Collisions were handled by the Schmidt-Rutland method [55] with O'Rourke's model [56] for collision outcomes. Parcel-wall interaction, including wall-film formation and liquid-film dynamics on the piston, liner, and crevice surfaces, was modeled using O'Rourke splash and O'Rourke–Amsden separation [57]. Turbulence was modeled with the RNG k-ε approach [58].

For the auxiliary reactive closed-cycle validation discussed later in Section 3.1, combustion chemistry relied on the SAGE chemistry model [59]. Within that framework, n-dodecane oxidation followed Yao et al.'s reduced kinetics [60]; and NOx formation was modeled using the thermal NOx (extended Zeldovich) mechanism [61]. The combustion model comprised a total of 296 reactions among 54 species.

Adaptive mesh refinement (AMR) [62] was based on local temperature gradients, with a maximum embedding level of 3 and a subgrid threshold of 2.5. Fixed refinement covered the spray region, piston bowl, crevices, and liners at simulation start. A 0.008 m base grid spanned the remainder of the domain. Separate embedded meshes were created for each of the nine injector holes, each tied dynamically to the fixed background mesh, to capture unique spray patterns from each hole. Within the SAGE framework, chemistry calculations were solved using the CVODES dense solver. Fig. 1 depicts the geometry of the chamber and injector locations. Appendix A illustrates the CFD-to-zonal fuel-distribution post-processing workflow.

2.3. Reduced-order spray model (ROSM): Equations and assumptions

This study used the Musculus and Kattke model [45] as the baseline approach for modeling spray formation and post-end of injection (EOI) mixing in RCCI conditions. Among the classical phenomenological models reviewed in the introduction, this model offers a good balance between physical accuracy and computational efficiency. It accounts for transient effects such as multiple injections and rate shaping, and it captures the entrainment-wave behavior after EOI, which is relevant to late-stage spray evolution and RCCI mixture stratification. Compared to other models, it provides greater flexibility for adjusting input parameters and has been widely validated in the literature [45]. Nevertheless,

Table 2
Geometry of the diesel injector nozzle.

Nozzle	Parameters	Value/Units
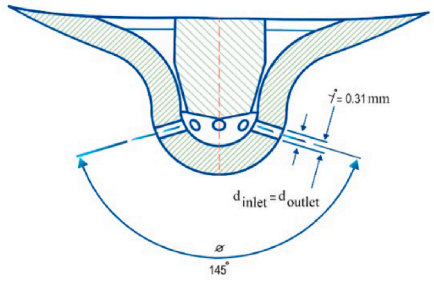	Number of holes Hole diameter (Ø) Umbrella angle (φ°) Nozzle K factor	9 0.31 mm 145 degrees $K = \frac{dinlet - doutlet}{10}$
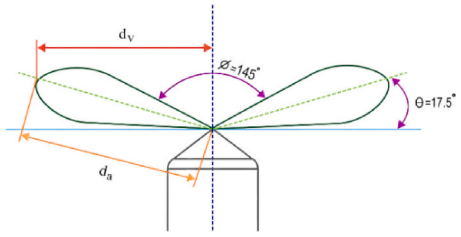	Schematic side view of the multi-hole (MH) injector spray (illustration not to scale) approximate penetration length (da) visually observed penetration length (dv)	

Table 3
Light fuel oil (LFO) properties from the supplier's certificate of analysis (COA).

Parameter	Unit	Value
Fuel oil carbon	% mass	87.7
Fuel oil hydrogen	% mass	14.6
Fuel oil sulphur	% mass	0.001
Fuel oil nitrogen	% mass	0.1
Fuel oil water content	% volume	0.01
Fuel oil stoichiometric air/fuel ratio	kg/kg	15.1
Fuel oil stoichiometric dry air demand	Nm^3/kg	11.68
Fuel oil lower heating value	MJ/kg	42.95
Calculated cetane index	No unit	6.7
Flash point	∘C	64.5
Sulfur (low level)	mg/kg	< 10

Table 4
Specification of sub-models and governing assumptions used in CFD simulation.

Physical process	Model	Governing parameters / assumptions used here
Diesel fuel injection	Lagrangian parcel modeling	9 holes; hole Ø = 0.31 mm; umbrella angle φ = 145°; K-factor = 0 (cylindrical); injector orientation α = 17.5°; rail pressure 1399 bar; injection duration 4575 μs; injector at 300 K; nominal spray cones as in Fig. 1.
Spray droplet breakup	KH–RT (modified)	No prescribed breakup length; KH/RT constants: solver defaults.
Droplet evaporation	Frössling correlation	Property-coupled evaporation using fuel/gas thermophysical properties; non-reactive and hot/cold modes as configured.
Droplet collision	Schmidt–Rutland (NTC)	No-time-counter collision frequency; solver-default parameters
Collision outcomes	O'Rourke	Coalescence/bounce/splash criteria: solver defaults.
Drop/wall interaction	O'Rourke splash + O'Rourke–Amsden separation	Wall film enabled; wetness/contact angle/splashing models
Turbulence	RNG k–ε	Model constants and turbulent Pr/Sc numbers: solver defaults.
Heat-transfer	O'Rourke–Amsden	Wall/convective heat-transfer closure: solver defaults.
Combustion chemistry	SAGE	Reactive closed-cycle validation only; mechanisms: Yao et al. (n-dodecane surrogate) + thermal NOx (extended Zeldovich); 54 species / 296 reactions
Mesh & AMR	Base mesh + AMR + separate embedded mesh per nozzle	Base cell size = 0.008 m; AMR max level = 3; sub-grid threshold = 2.5; fixed refinement in spray region, bowl, crevices, liners; separate embedded mesh per nozzle.

besides the simplified spray-angle treatment, the model also involves reduced-order assumptions that may constrain its applicability under early-injection, low-load, low-density conditions. In the present study, these limitations are explicitly acknowledged and accepted within the intended accuracy–computational efficiency trade-off, as the model is used as a benchmark rather than a universally applicable description.

The reduced-order spray model (ROSM) built upon this framework was developed for efficient simulation of fuel mixing behavior after EOI. It enables faster simulations than full CFD, while retaining key physical characteristics relevant to early injection strategies. Appendix B provides details of the MATLAB code structure model.

Following Musculus et al., the ROSM models the diesel jet as a sequence of discrete control volumes (CVs) with a prescribed spreading angle.

Fig. 2 illustrates the CV discretization and notation. The model computes fuel mass and axial momentum along the jet during injection and through the post-EOI transient. The spray model adopts the following governing assumptions:

- The model treats the fuel jets as non-vaporizing, but can still forecast mixing-restricted vaporization behavior.
- The flow is incompressible. Due to high speeds, compressibility can be significant near the nozzle of a diesel jet, but its effects are minimal in the slower flow downstream.
- Viscous turbulent and molecular forces are overlooked as they are minor (vs. pressure forces). Shear forces are likewise disregarded (at the jet boundary) due to small velocity gradients. In contrast, noticeable shear forces within high-shear regions are confined to the CVs, and thus, the external forces are not affected.

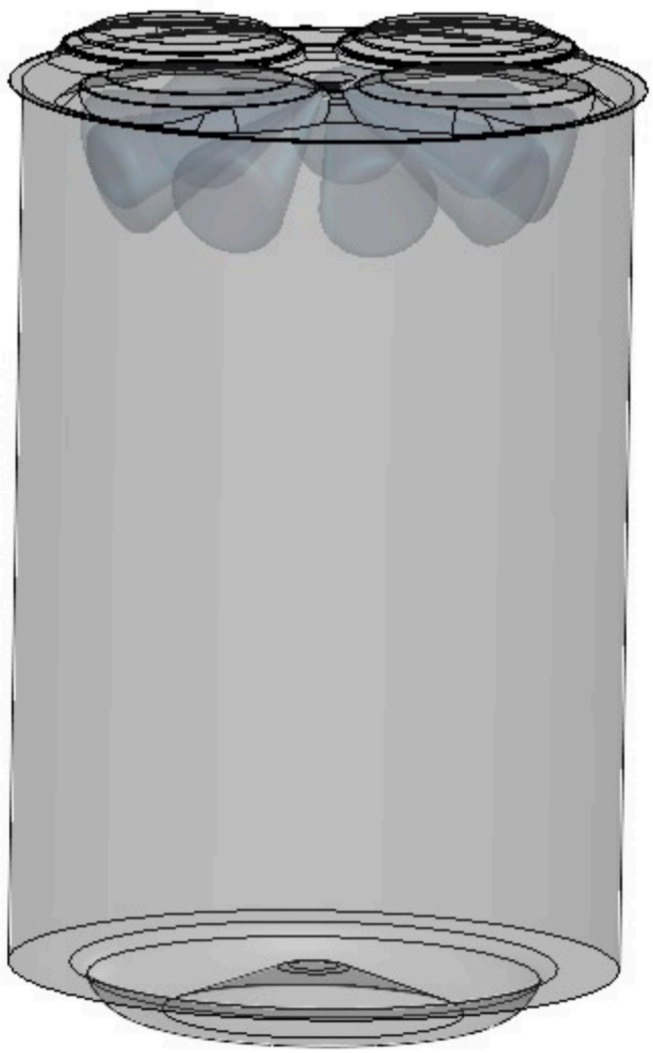

Fig. 1. Cylinder CFD (CONVERGE) domain showing the cylinder geometry, injector location, and nominal spray cones.

- The transient momentum equation solely considers axial convection and neglects the momentum axial mixing caused by turbulent and molecular diffusion.
- Axial pressure gradient forces are assumed to be negligible, which is reasonable for steady jets.
- The angle of jet spreading is assumed to be constant throughout and post-EOI transient. A constant angle is typical for steady jets, but it is uncertain if this holds during EOI, as ambient fluid might narrow the jet. Despite no theoretical proof, experimental evidence suggests that the angle of spreading remains nearly invariable or slightly upsurges throughout EOI.
- The mean axial velocity's radial profile stays unchanged during the EOI transient.

The mass of the fuel and the momentum are computed in each CV, using an upward differencing scheme. The discretized equations Eq. (1) and Eq. (2) define the evolution of fuel mass and momentum in individual CVs:

$$m_{f,i}^{t+1} = m_{f,i}^{t} + \rho_f \left(\left(\beta \overline{\overline{X}_f} + \overline{\overline{u}} A \right)_{i-1}^{t} - \left(\beta \overline{\overline{X_f}} \overline{\overline{u}} A \right)_{i}^{t} \right) \Delta t \tag{1}$$

$$M_{f,i}^{t+1} = M_{f,i}^{t} + \left(\left(\overline{\overline{\rho}} \beta \overline{\overline{u}}^2 A \right)_{i-1}^{t} - \left(\overline{\overline{\rho}} \beta \overline{\overline{u}}^2 A \right)_{i}^{t} \right) \Delta t \tag{2}$$

Note that, t represents the "time step," and i represents the CV index. The Courant-Friedrichs-Lewy (CFL) [45,63] condition determines the time increment (t) to ensure that the time step is small enough relative to control volume widths, so that the scheme remains stable. The spray's CVs take the same width. The model's key inputs are ambient density, temperature, fuel density, nozzle specification, and injection pressure. The model can predict the spray evolution for a transient injection rate, so real injection profiles can be provided as input to the model. Profile factor β in Eq. (1) and Eq. (2) serves two purposes: it links the fuel distribution and average velocity profiles to the combined profile average in Eq. (1); and behaves as a momentum-flux correction in Eq. (2), linking "averaged squared velocity" to the "square of averaged velocity" under invariable spray density [64]. The double bars in Eq. (1) and Eq. (2), u (spray velocity), X_f (fuel volume fraction), and ρ (spray density) denote the averaged time averages (for these values) over the spray's cross-section. A, defined according to Eq. (3), denotes the boundary area between CVs, at a distance x from the injector [64]:

$$A(x) = \pi \left(x \frac{\tan\theta}{2} \right)^2 \tag{3}$$

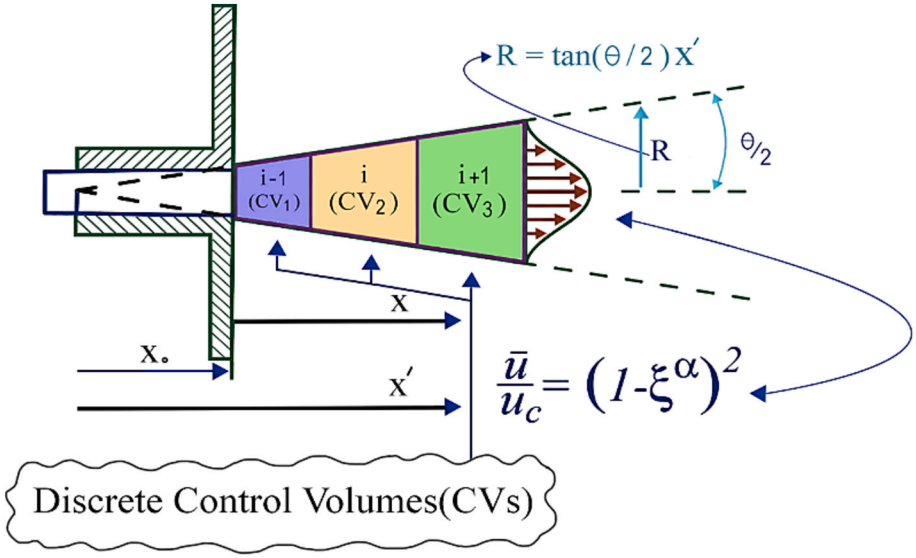

Fig. 2. Schematic representation of the Musculus spray model [45].

Table 5
Tuning parameters for sensitivity analysis.

Parameters	Physical interpretation	Calibration range
Gamma (γ)	A factor for phi-threshold (liquid penetration)	NA
Beta (β)	accounts for "velocity profile" and "fuel volume fraction shape"	1 (uniform profile) to 2 (entirely developed jet)
Alpha (α)	Describes profile evolution, i.e., from a top-hat, uniform form (at the nozzle) to an entirely developed form	0 (top-hat, uniform form at the nozzle) to ∞ (entirely developed form) [65]
C_a	Area contraction coefficient	0 (no flow—theoretical limit) to 1 (means no contraction—ideal case) [66]
A_c	Spreading angle correction factor	NA

In this case, the angle of spreading (for free spray), represented by θ, reflects the mixing rate with the surrounding fluid. A greater θ indicates a more effective mixing of ambient and injected gases [64]. The Siebers relations [37] compute θ, a key element in spray calculations. The θ value is considered to stay constant during and post-EOI in the Musculus spray model. However, experimental research implies that the θ value increases downstream and decreases near the nozzle exit. Predictions of spray penetration are enhanced by incorporating this variable behavior into the Musculus model [45].

Along the axis of the free spray, both the fuel volume fraction (Eq. (4)) and the turbulent mean velocity (Eq. (5)) are assumed to follow non-uniform profiles proposed by Abramovich.

$$\frac{\overline{X}_f}{\overline{X}_{f,c}} = (1-\xi^a)^2 \tag{4}$$

$$\frac{\overline{u}}{\overline{u}_c} = (1-\xi^a)^2 \tag{5}$$

The centerline values are related to the cross-sectionally averaged fuel volume fraction $\overline{\overline{X}_f}$ and velocity $\overline{\overline{u}}$ by Eq. (6) and Eq. (7):

$$\overline{\overline{X}_f} = \frac{\int \overline{X}_f dA}{\int dA} = \frac{\alpha^2}{(\alpha+1)(\alpha+2)}\overline{X}_{f,c} \tag{6}$$

$$\overline{\overline{u}_f} = \frac{\int \overline{u}_f dA}{\int dA} = \frac{\alpha^2}{(\alpha+1)(\alpha+2)}\overline{u}_c \tag{7}$$

β is derived from α, and α itself comes from an empirical equation that links to velocity and fuel disturbance. The parameter β is computed, based on Eq. (8):

$$\beta = \frac{6(\alpha+1)(\alpha+2)}{(3\alpha+2)(2\alpha+1)} \tag{8}$$

where c in Eq. (4) and Eq. (5) represents values over the centerline of the spray jet, and ξ is the non-dimensional radial position, in which $\xi = r/R$ represents the "radial coordinate/jet width" ratio. Likewise, α (an adjustable parameter) enables profile transition from a "top-hat shape" (at the nozzle) to an "entirely developed form" downstream. The profile resembles a Gaussian error function with $\alpha = 1.5$ in an entirely developed jet. Higher α values (α:∞) result in flat profiles close to the nozzle. In the transition region, α is adjusted to ensure the centerline velocity does not exceed the nozzle exit velocity. The model's boundary condition is the jet's velocity at the nozzle, u_0 [45,64]. The first CV is initialized before solving the mass and momentum equations. At the beginning of injection, the fuel volume fraction is set to "1" since this control volume is expected to be filled with fuel. The fuel volume in the cell is calculated from this volume fraction, and the jet velocity is taken as the nozzle exit velocity. Next, this velocity calculates the fuel momentum in the first control volume. Mass and momentum (in each CV) are iteratively solved over each time step. Jet velocity and the cross-sectionally averaged fuel volume are determined accordingly [45].

2.4. Calibration and validation

This section defines the calibration–validation workflow used to assess the ROSM against CFD. We first specify the zone-based targets and the mapping from control volumes to engine-relevant zones (Section 2.4.1). We then identify and bound the tunable parameters via sensitivity analysis (Section 2.4.2, Table 5). Calibration uses a design of experiments (DOE)-driven optimizer on 67% of the operating points to minimize errors in penetration and zonal fuel distribution, followed by validation on the remaining 33% (Section 2.4.3, Table 6). Finally, the experimental basis and the strategy for adopting CFD as the high-fidelity reference are summarized in Section 2.4.4.

2.4.1. Developing zonal fuel distribution

The main objective is to quantify fuel distribution across zones in the combustion chamber. Here, spray control volumes (CVs) denote the discrete elements used by the ROSM along the spray axis, whereas zones denote the cylinder-fixed regions used in CFD post-processing to characterize in-cylinder stratification. The CFD framework partitions the chamber into concentric cylindrical zones about the cylinder's central axis. However, in this study, the spray is injected at $\theta = 17.5^\circ$ relative to the cylinder surface and the numerical model defines CVs perpendicular to the spray axis, so fuel mass in CVs is evaluated in a coordinate system which differs from the cylinder-fixed zonal system. Moreover, fuel is not uniformly distributed within each CV (mass is typically higher near the centerline than at the periphery), which makes the mapping from CVs to zones non-trivial. Fig. 3 depicts three methods which were considered to calculate the zonal fuel distribution from the CV-based distribution in the code. The first method assumes that the CVs are parallel to the chamber zones, making the calculations straightforward. This assumption is computationally less demanding, but does not fully capture real spray geometry. The second method introduces angled CVs which match the actual spray angle, improving alignment with the physical behavior of the spray. However, it assumes that the fuel is uniformly distributed within each CV, which does not accurately represent the inhomogeneous mixing and the centerline-peaked fuel concentration observed in real sprays. The third method also uses angled CVs, but applies a non-uniform fuel distribution within each CV. Instead of assuming fuel spreads evenly, it accounts for variations in concentration, thus better reflecting the physical behavior of fuel spray. This study selected the non-uniform mass distribution model (Fig. 3 (c)) because it extracts fuel distribution values more accurately, closely aligning with the actual fuel distribution.

2.4.2. Tuning parameters

After developing the phenomenological spray model, including zonal distribution calculations, a sensitivity analysis was conducted to identify tuning parameters for model calibration and validation. The tuning process avoids altering physical inputs, focusing instead on parameters explicitly intended for calibration. Relevant parameters are systematically varied to assess their impact on model outputs, like spray penetration and fuel mixture distribution. This iterative sensitivity analysis process ensures that the most relevant and effective parameters are selected. Table 5 lists the initial candidates for tuning parameters, together with their physical interpretation and feasible calibration range.

Table 6
Operating points and inputs for model calibration and validation. Δθ_inj is the injection duration in crank-angle degrees; ρ_a and T_a are the in-cylinder mixture density and temperature at SOI; SOI is referenced as crank angle before TDC (°CA bTDC).

Case	Injection duration (degree)	mixture density kg/m^3	mixture Temperature K	SOI [∘ CA bTDC] degree	
A mid	ref + 1.5	ref + 5.54	ref + 211	ref + 31	Calibration
B high	ref + 0.3	ref + 8.39	ref + 179	ref + 28	
C low	ref + 0.1	ref + 1.75	ref + 237	ref + 36	
D	ref + 0.0	ref + 8.38	ref + 255	ref + 17	
E	ref − 0.1	ref + 7.07	ref + 224	ref + 23	
F	ref − 0.1	ref + 4.45	ref + 157	ref + 41	
G	ref + 0.5	ref + 5.14	ref + 176	ref + 35	Validation
H	ref + 0.0	ref + 6.04	ref + 199	ref + 29	
I	ref − 0.1	ref + 3.95	ref + 141	ref + 47	

ref: 25% load operating point of a commercial, conventional dual-fuel version [67] of the experimental engine. For mixture density and temperature, ref denotes the intake manifold density and temperature at this operating point.

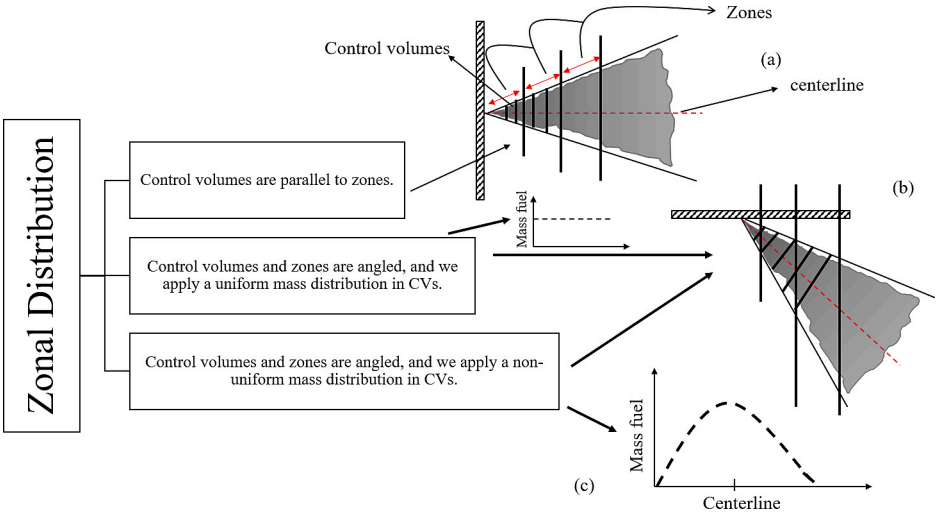

Fig. 3. Different methods for mapping zonal distribution based on CFD results: (a) Control volumes are parallel to zones; (b) mass distributed uniformly; (c) mass distributed non-uniformly.

2.4.3. Optimizer and design of experiments (DOE) for local/global tuning

The calibration and validation procedures were based on nine CFD operating points, representative of different injection and mixture conditions for the W6L20 engine. These cases were divided into a 67%/33% split, with six cases (cases A to F) used for calibration and the remaining three reserved for validation. The goal was to determine tuning parameters that minimize the difference between model predictions and CFD results in both zonal fuel distribution and spray penetration. Table 6 summarizes the operating conditions for all cases. Appendix B describes the two-stage model calibration procedure. In Stage 1 (local tuning), a design of experiments (DOE) approach was used to generate a set of parameter samples within the defined calibration ranges. Given the dimensionality of the parameter space, Latin hypercube sampling (LHS) was employed to ensure efficient and uniform coverage of the input domain [68]. For each calibration case, the optimizer evaluated every sample by computing (i) the mean squared error (MSE) of the fuel-distribution profile; and (ii) peak metrics, including the magnitude and location of the maximum fuel fraction. The parameter set that minimized the aggregate error was selected as the locally optimal solution for that case. In Stage 2 (global tuning), a single set of parameters was optimized to minimize the total error across all calibration cases. This global solution serves as a universal calibration for the W6L20 engine and prioritizes generality over perfect case-by-case fit. Although global tuning may reduce case-specific accuracy slightly, it improves robustness and applicability across a wider range of conditions.

2.4.4. Validation framework and CFD reference strategy

Direct spray-tip penetration measurements were available only for **Case A**, obtained in the optical constant-volume chamber. Because the reduced-order spray model developed here must reproduce not only penetration but also cylinder-fixed zonal fuel distribution across multiple operating conditions, direct calibration against experiment alone was not feasible for the full dataset. Therefore, after validation against the available spray and closed-cycle engine measurements, the CFD framework was adopted as the high-fidelity reference for ROSM calibration and validation. Penetration was compared between CFD and chamber measurements obtained by high-speed Schlieren imaging, which resolves density-gradient contours during diesel injection and mixing. Spray penetration length is defined here following Zhou et al. [69] as the axial distance from the nozzle tip to the point enclosing 99% of the projected spray area. This approach avoids the common overestimation that can occur when measuring to the farthest visible droplet, which may represent isolated outliers rather than the main spray structure [70].

3. Results and Discussion

3.1. CFD model validation with experimental data

Fig. 4 shows the nine experimental nozzle traces, their mean, and a pooled nozzle-to-nozzle tolerance band for SOI to 10 crank angle after

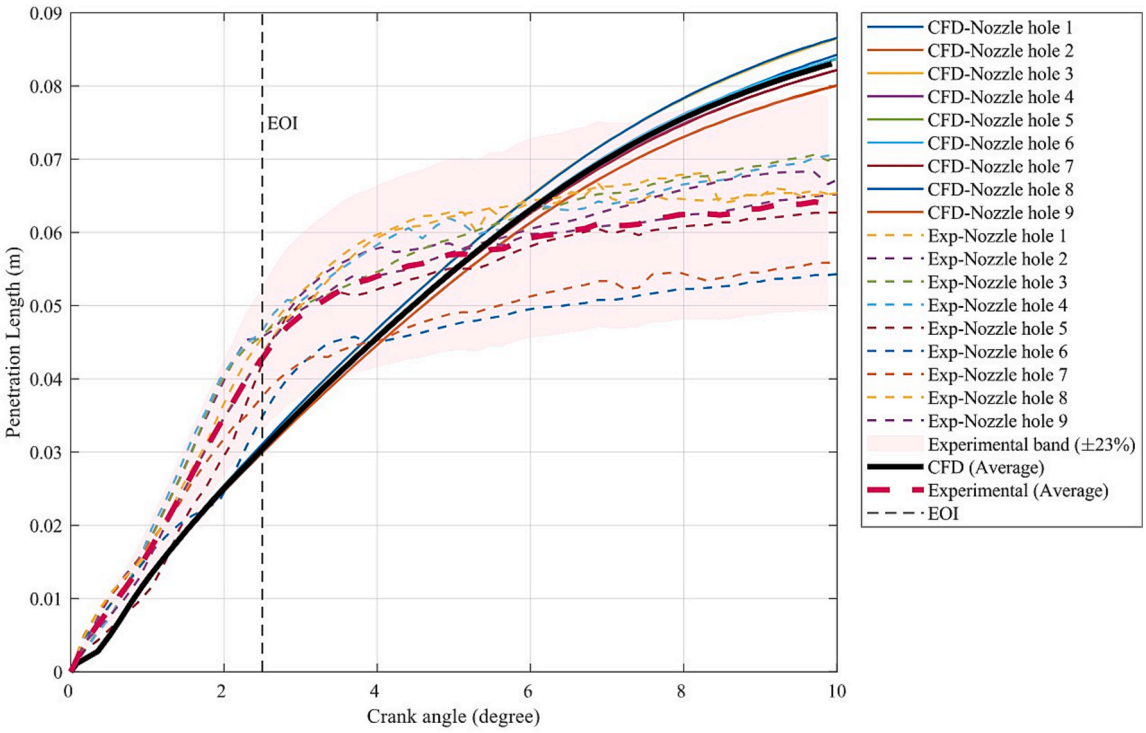

Fig. 4. Comparing penetration length of CFD (Case A) with experimental data for nine nozzle holes.

SOI. The band is the 97th-percentile of the pooled absolute relative deviations of each nozzle's penetration from the experimental mean (±23%), i.e., it represents the production-tolerance spread among nominally identical nozzles. Segmenting by end of injection (EOI) clarifies where differences arise. Pre-EOI, the CFD underpredicts early growth and lies within the band for 26.7% of samples, with mean absolute percentage error (MAPE) ≈ 31.3% and root-mean-square error (RMSE) ≈ 0.0069 m. This degradation is consistent with well-known sensitivities in the needle-opening/near-nozzle phase: small uncertainties in effective orifice coefficients and primary-breakup timing (e.g., KH-driven atomization onset) disproportionately affect the first frames. Additionally, tip detection at very low penetration is more susceptible to thresholding noise. Post-EOI, once the jet is established, the CFD tracks the ensemble trend substantially better: 66.7% of samples fall within the ± 23% band, with MAPE ≈ 17.1% and RMSE ≈ 0.0113 m. The remaining late-segment spread is plausibly linked to the breakup-model sensitivity governing atomization rate and thus the penetration trajectory. Employing the 97th-percentile nozzle-to-nozzle tolerance band (±23%), the CFD penetration for Case A satisfies the overall validation criterion over SOI to 10 crank angle later (within-band coverage

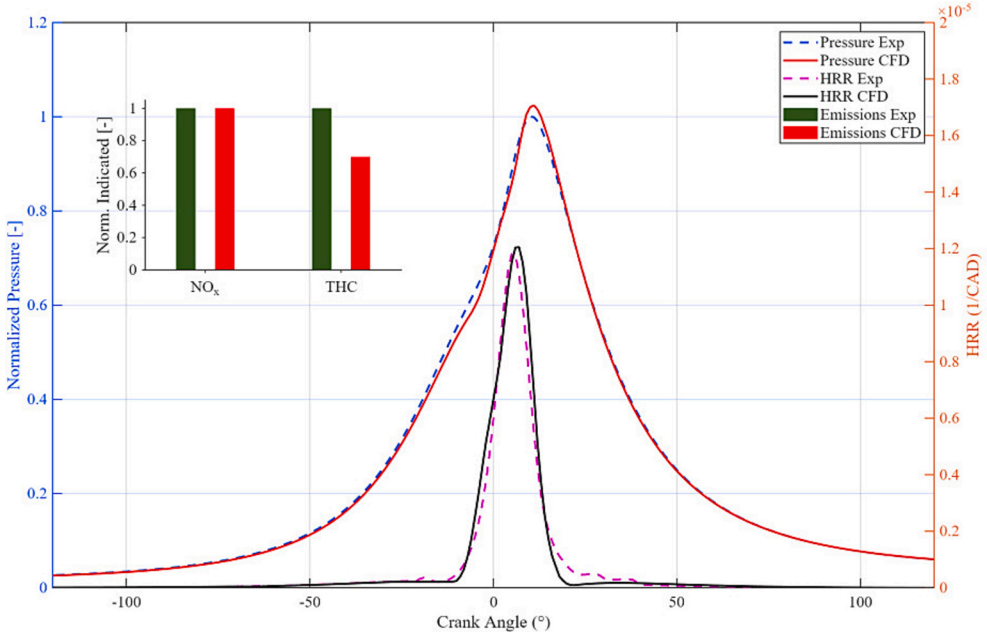

Fig. 5. Comparison of experimental and simulated heat release rate (normalized by the total fuel energy), in-cylinder pressure (normalized by the experimental peak pressure), and emissions for a representative mid-load RCCI case (CASE A).

≈ 56.1%; MAPE ≈ 20.7%; RMSE ≈ 0.0103 m). Our target comparison region for ROSM use is post-EOI and pre-impingement: agreement in this range is strong (within-band coverage ≈ 66.7%). We acknowledge weaker behavior in the pre-EOI phase (within-band coverage ≈ 26.7%), which lies outside the tuning focus. Accordingly, we consider the CFD solution validated and use it as the reference for subsequent zonal mapping and ROSM calibration.

For the closed-cycle validation, Case A was simulated from IVC to EVO and compared with W6L20 measurements under matched conditions. The charge at IVC comprised air with homogeneously premixed CH_4/C_2H_6, and a light fuel oil (LFO) pilot provided the high-reactivity source. The initial mixture was taken as spatially uniform with a swirl ratio of 2.0:1, and the SOI and injection duration were matched to the experiment at the same operating point [71]. Fig. 5 illustrates in-cylinder pressure (experimental and numerical) and HRR traces for a mid-load case. Model results agree well with experimental data for these operating conditions. Assuming a + 4.2 bar absolute error, the peak pressure was predicted, and the peak pressure was positioned within 1 CAD, both with 2.5% accuracy (Pmax_sim/Pmax_exp = 1.025). This implies that simulation results are satisfactorily accurate in predicting the engine's key performance parameters. Furthermore, the RMS error was ~ 1.15 bar (for predicted pressure with the experimental one) and 0.0476 kJ/s (for HRR) [10].

As shown in Fig. 5, NOx emission closely matches experimental results, with only a 1% relative error, implying satisfactory agreement between the model and experimental data. The model predicts total hydrocarbon (THC) emission with slight variations, which are reasonable and acceptable.

In addition to the representative Case A comparison shown in Fig. 5, the same combustion-oriented validation procedure was also checked for Cases B and C in terms of pressure and HRR behavior. While direct spray-penetration measurements were available only for Case A, these additional combustion-level comparisons support the consistency of the adopted CFD framework across representative operating conditions. Taken together, the available spray and closed-cycle evidence justify the use of CFD as the high-fidelity reference for subsequent zonal mapping and ROSM calibration/validation.

3.2. Mapping of 3D fuel distribution into quasi-dimensional zones: Method comparison

The analysis is restricted to the free-field spray regime prior to wall impingement, as the ROSM model currently does not account for wall interaction. For each case, the comparison instant is defined as the last timestep before wall interaction, approximated when axial penetration reaches ≈0.8–0.9 of the available spray length. For cases where this condition is not met before start of combustion (SOC), the SOC instant is used (Case C). Appendix A illustrates the CFD process and solver structure. The complete CFD contour sequence for Case A, showing the diesel-jet evolution from SOI to SOC and the free-field region considered in the present analysis, is included in Appendix E.

Using these reference points, zonal fuel distributions from CFD are compared against ROSM predictions using the three mapping methods (Methods 1–3) for representative operating conditions (Cases A–C: mid-, high-, and low-load). The results, shown in Fig. 6, present the cylinder-fixed zonal distributions (Zones 1–10) together with the corresponding in-cylinder flow fields.

Across all three operating points, the CFD reference shows a mid-spray maximum with lower fractions near the injector and tip. Across all loads, Methods 1 and 2 systematically shift the peak fuel-fraction downstream relative to CFD, while Method 3 preserves the peak location but overstates its amplitude. The downstream bias of Method 1 arises from ignoring spray inclination in the CV–zone mapping, whereby CV centroids lie along the spray-aligned coordinates but are mapped as if s ≡ x, the cylinder-fixed axial coordinate. The correct projection is x = s cos θ, where θ is the angle between the injection axis and the cylinder

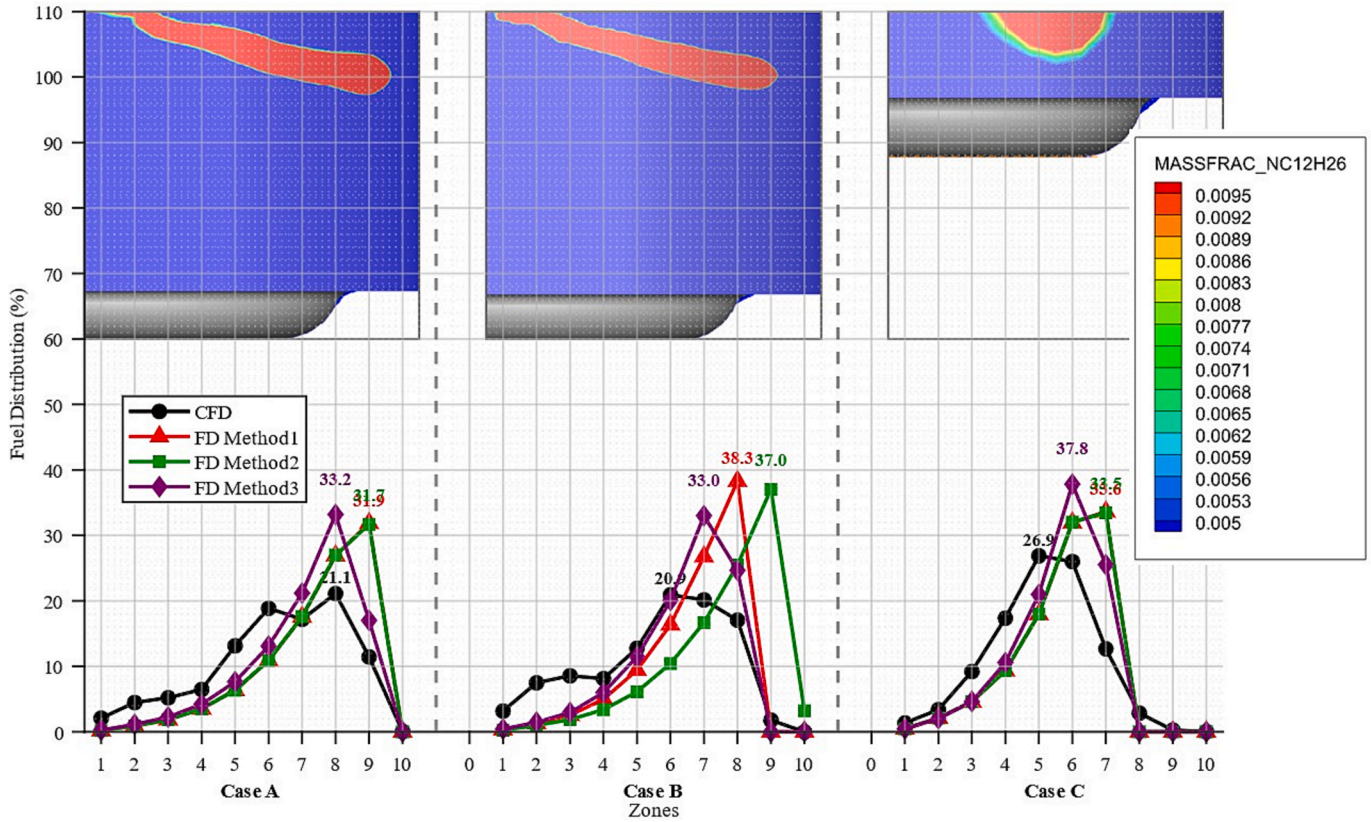

Fig. 6. Zonal fuel distribution for Cases A–C at the target crank angle (pre-impingement): CFD vs Methods 1–3.

horizontal. Neglecting this introduces a systematic positive error $\Delta x \approx s(1 - \cos\theta)$ which grows with penetration length s and with θ, hence the increasing downstream index shift at higher-momentum (longer-penetration) conditions. Method 2 introduces bias by treating each control volume as uniformly filled. As the inclined, widening jet is mapped onto cylinder-fixed zones, the overlap with later zones lies mainly in the CV's outer rim, where the true fuel fraction is low. The uniform assumption over-credits that rim, so downstream zones accumulate excess mass and the apparent peak shifts downstream. Method 3 correctly preserves the peak location by using a center-weighted in-CV profile. However, a residual peak-magnitude bias persists for two reasons: (i) the centerline-weighted profile, while more realistic than a uniform fill, only approximates the CFD-resolved mass field; and (ii) the ROSM concentrates a large fraction of fuel into a few CVs near the advancing jet front (≈80–90% of the penetration length), whereas CFD distributes mass more broadly in that area. Consequently, downstream zones are over-credited and the peak magnitude is overstated despite the correct location. Peak location is more consequential than peak height for ignition-sensitive predictions. Shifting the peak downstream distorts local stratification and the emergence of auto-ignition kernels, propagating to HRR phasing and emissions. We therefore adopted Method 3 to preserve the peak location, while acknowledging a systematic overestimation of peak magnitude. This amplitude bias appears in the accuracy of the model's predicted maximum fuel-distribution (FD) value. However, we accept this trade-off in the present analysis because ignition sensitivity is governed primarily by the spatial placement of the maximum.

3.3. ROSM sensitivity analysis

Only three parameters of the considered candidates proved effective for calibration under the present conditions: the area–contraction coefficient Ca, the momentum–flux correction factor β, and the velocity–profile evolution exponent α. Other candidates showed negligible impact on the evaluated outputs and were not pursued further. Relative sensitivities were computed around the baseline parameter set by perturbing each parameter by ± 10%, ±20%, and ± 30%, and measuring the normalized response of three outputs: (a) maximum fuel fraction (peak HRF), (b) peak–zone location (zone index of the maximum), and (c) spray penetration length at the target crank angle (pre–impingement/SOC as per Section 3.2). The sensitivity metric was the absolute, normalized finite–difference ratio $|\Delta y/y| \,/\, |\Delta p/p|$, evaluated independently for each parameter level. Fig. 7 summarizes the results, which are as follows:

- Global ordering. Across the evaluated perturbations, sensitivities follow Ca, $\beta \gg \alpha$ with output–specific emphasis: peak fuel fraction $\beta > Ca \gg \alpha$; peak–zone location $Ca \approx \beta \gg \alpha$; penetration length $\beta \geq Ca \gg \alpha$. This is consistent with a momentum–controlled regime at the selected pre–impingement crank angle.
- Penetration (c). Increases in β (a more center–peaked exit profile) and Ca (larger effective discharge area) both raise the axial momentum flux, lengthening penetration. The β effect appears stronger or comparable to Ca because it concentrates momentum in the jet core and reduces near–field entrainment losses. The α exponent, governing radial–profile curvature, modestly alters shear–layer development and mixing but has only a small impact on axial reach at this time slice.
- Peak fuel fraction (a). β dominates the peak because it intensifies core focusing and mass–flux shaping, elevating the local HRF maximum. Ca also increases the peak by boosting total/axial momentum, whereas α slightly smooths the radial distribution (flatter core–edge contrast), yielding a small but non–zero reduction in peak amplification.
- Peak zone location (b). Both Ca and β drive the rich core downstream, shifting the peak to larger zone indices through increased reach and sustained core momentum; α remains negligible for location. Location is a discrete index, so the apparent sensitivity can change in steps and may plateau once the maximum has crossed a zone boundary.

These results provide the following implications for calibration. Ca and β are the primary levers. Ca sets momentum–consistent reach and penetration, while β controls stratification intensity and core coherence. α is retained as a fine–tuning parameter to smooth radial profiles (reduce excessive core peaking) without materially relocating the peak, thereby avoiding overfitting of location–sensitive metrics. These trends are consistent with established experimental and modeling findings for diesel sprays [38,72]. Additional sensitivity checks were also carried out for representative low-load and high-load cases. These confirmed that the same dominance order is preserved across the studied operating range, with Ca and β remaining the primary sensitivity levers and α retaining a secondary role. Although the relative sensitivity magnitudes vary quantitatively with operating conditions, the overall ranking remains unchanged.

3.4. ROSM calibration: local vs global

Before examining local and global calibration outcomes, we first

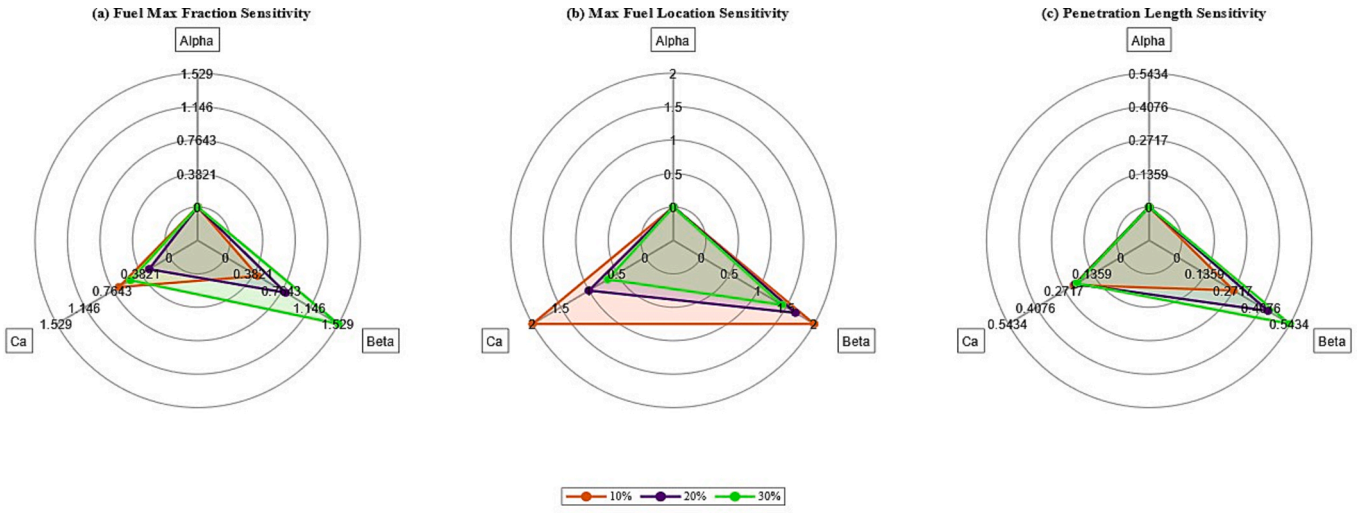

Fig. 7. Relative sensitivities (Case A) of ROSM outputs to ± 10/20/30% perturbations in Ca, β, and α: (a) maximum fuel fraction; (b) peak-zone location; (c) penetration length at the target crank angle.

verified that the zonal fuel distribution (FD) metric is robust with respect to the number of zones used to discretize the cylinder.

Fig. 8 quantifies the sensitivity of the predicted location of the peak–fuel zone to the zonal resolution for Case E, with N ∈ {10, 50, 100} and both global and local calibrated parameter sets. For each N, we compute the index offset between the model and CFD at the zone of maximal fuel and normalize it by N. The global calibration yields normalized errors of 0.10, 0.10, and 0.08, while the local calibration gives 0.10, 0.08, and 0.13 for N = 10, 50, 100, respectively. Thus, across a tenfold change in N, the discrepancy remains confined to 0.08–0.13, with no monotonic trend versus resolution. Variability is small for both calibrations. The slight deviation at N = 100 is consistent with peak flatness and boundary discretization (adjacent zones of nearly equal fuel content) rather than a systematic bias. Thus, the peak–location metric is effectively resolution–independent. Increasing N only refines discretization without changing relative misalignment, providing a robust basis for the tuning/calibration process.

To expose the calibration process and the structure of the error landscape, Fig. 9 shows parallel-coordinates views for a mid-load case (A) and a low-load case (C). The first three axes are the tuning parameters (α, β, Ca); the remaining four axes are errors with respect to CFD, namely penetration-length error, peak-zone (FDM) error, peak fuel-fraction error, and the aggregate mean-squared error (MSE). DOE candidates are drawn as semi-transparent polylines, with the black polyline marking the local optimum for the case, and the green polyline the global optimum used across cases. Because the four right-hand axes are errors, desirable solutions lie near their lower bounds. In Case A (mid load), the candidate bundle visibly narrows across the error axes: points that minimize penetration error also tend to yield small location and peak-fraction errors, indicating a positive correlation among metrics. A corridor of near-optimal solutions appears where increases in Ca (reducing penetration error) are compensated by modest decreases in β (limiting over-focusing of the core), or other combinations. This low-error manifold indicates that many Ca, β, α combinations achieve comparably small residuals. Therefore, a single global parameter set has a higher probability of falling within this basin across multiple operating points, delivering acceptable errors simultaneously even if it is not individually optimal for any one case.

In Case C (low load), the geometry of the plot is qualitatively different. The polylines fan out and cross between the penetration, location, and peak-fraction error axes. Parameter moves that reduce penetration error frequently worsen either the peak location or the peak fraction. The metric correlations are weak or even opposing, revealing a conflicted calibration landscape with sharper trade-offs. Here, achieving acceptable penetration requires parameter combinations which tend to increase the other three errors; α again has little leverage. This ill-conditioning identifies Case C as an outlier from a calibration perspective and foreshadows the larger discrepancies observed later for low-load conditions. Overall, the parallel-coordinates analysis demonstrates that (i) parameter interactions generate families of acceptable solutions (useful for global calibration) in well-conditioned cases like A, and (ii) metric decoupling at low load (Case C) limits simultaneous error reduction. These observations provide the foundation for the subsequent local-versus-global comparison, where we quantify how these landscapes translate into predictive performance.

Fig. 10 summarizes the performance of the locally and globally calibrated ROSM for three representative operating points (Cases A, C, and E). Each row reports tip–penetration history (left) and zonal HRF distribution (right) at the target pre–impingement instant. The legends list the calibration coefficients associated with each solution.

For Case A (mid load), both calibrations reproduce the temporal evolution of penetration and the overall HRF shape. The local set reduces errors across metrics and places the HRF maximum at the correct zone, albeit with an overestimated peak amplitude. The global set tracks the penetration history closely but shifts the HRF peak one zone upstream, with a lower magnitude. Parameter values indicate convergence toward higher Ca and β in the local solution relative to the global set, consistent with the need for stronger core momentum to match both reach and stratification.

In Case C (low load), penetration and mixture-fraction metrics decouple. Combinations that limit penetration tend to misplace or depress the HRF peak, and vice versa. In the figure, the global set produces excessive penetration and a downstream-biased, diluted HRF peak, while the local set curtails penetration but shifts the HRF maximum upstream and amplifies it. Early in the event, the locally tuned penetration follows the CFD trajectory, after which the CFD curve bends toward a different regime which the phenomenological model cannot reproduce. This is consistent with a transition from purely momentum-

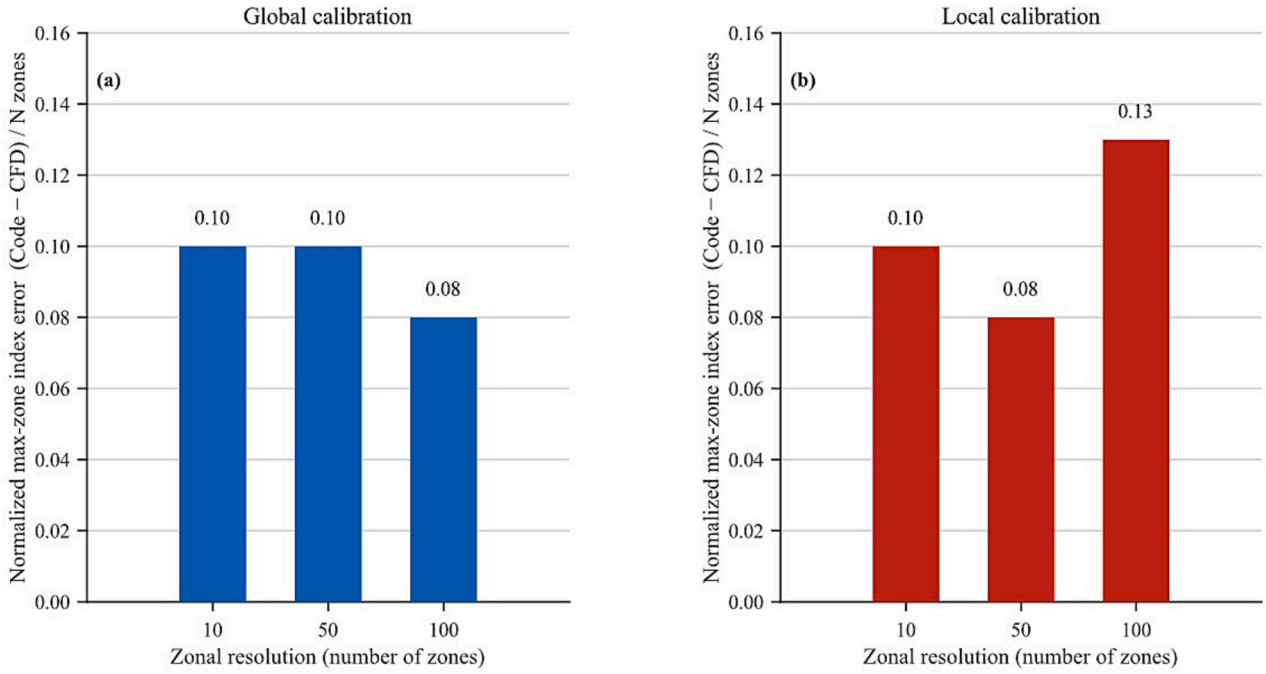

Fig. 8. Normalized peak-zone index error vs. zonal resolution (Case E) for global (a) and local (b) calibrations at N = 10, 50, and 100.

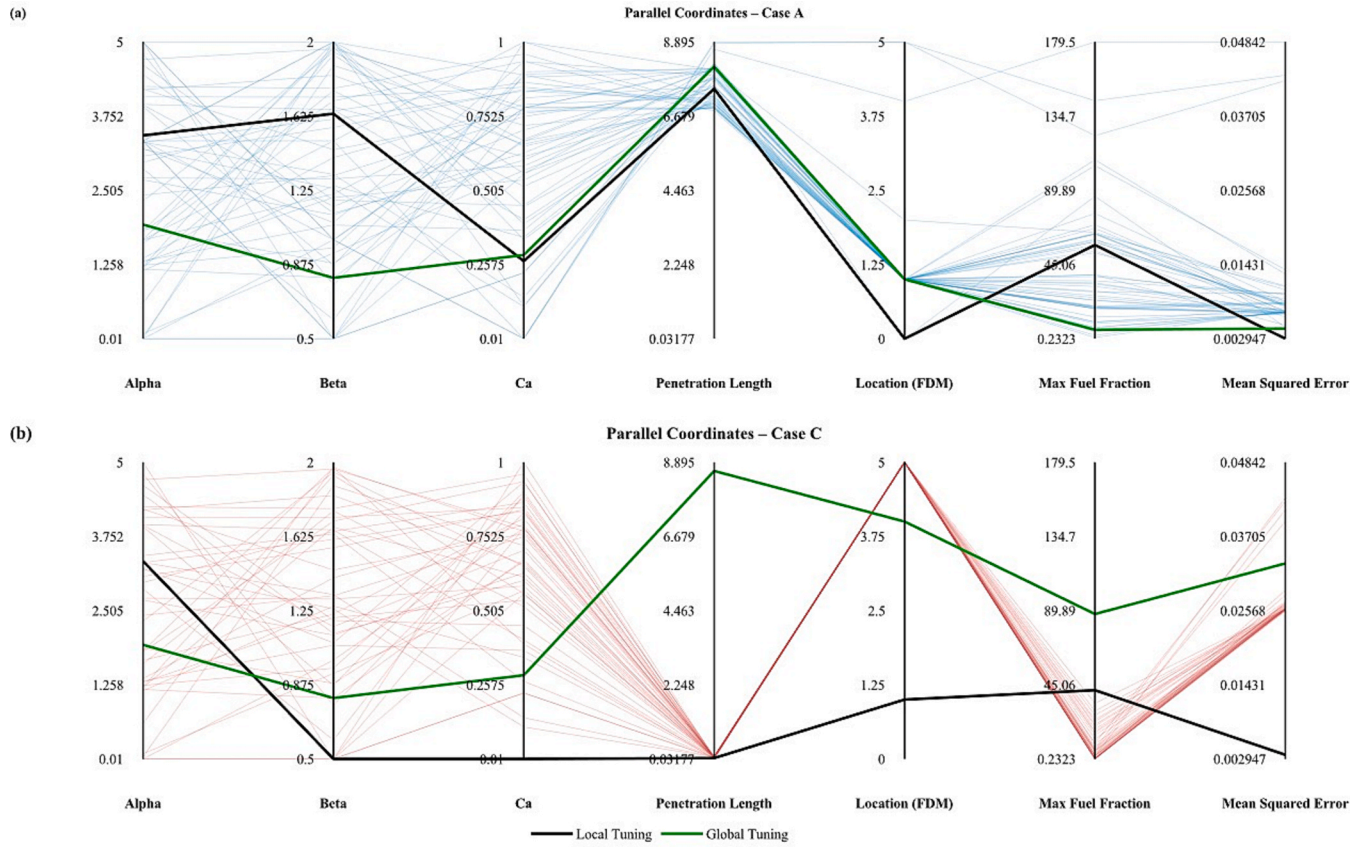

Fig. 9. Parallel-coordinates plots for Cases A and C, linking tuning parameters (α, β, Ca) to model–CFD errors (penetration, peak zone, peak fraction, MSE). DOE candidates are shown as light polylines; local and global optimal sets are highlighted in black and green respectively. (For interpretation of the references to colour in this figure legend, the reader is referred to the web version of this article.)

controlled development to mixing/evaporation-limited behavior under low ambient density. The coefficients reflect the conflict: the locally tuned Ca is about an order of magnitude lower than in other cases (~0.01 versus 0.1–0.5), indicating that matching penetration would require an unrealistically small effective discharge area and hence a different physics set. In this case, the CFD results indicate that spray development departs from the trend captured by the phenomenological model after the initial penetration stage. This deviation is associated with the low ambient-density environment of the low-load condition, which promotes an earlier transition from momentum-dominated spray evolution to a regime increasingly governed by mixing and evaporation effects. As a result, the governing assumptions of the present momentum-based framework become less valid for Case C, justifying its exclusion from the common calibration set. For Case E (high load), both solutions capture the trend of the penetration history but overpredict tip reach and place the HRF peak one zone later than CFD. The local set yields a higher peak magnitude than the global one. The local parameters ($\alpha \approx 4.03$, $\beta \approx 0.58$, $Ca \approx 0.47$) indicate a substantially larger effective discharge area and weaker momentum focusing than the global set ($\alpha \approx 1.93$, $\beta \approx 0.81$, $Ca \approx 0.21$). This reflects the broader tuning–interaction band noted earlier. Although the global set uses a lower Ca than the local one, concurrent adjustments in β and α partially compensate, so the overall match remains acceptable. In general behavior, the response to local versus global tuning mirrors Case A: the local set reduces errors across metrics while the global set offers an acceptable compromise.

Across the broader calibration set (Cases A–F), the cases not shown exhibit behavior analogous to A or E, for which the global parameter set provides acceptable errors while the local set reduces them further. Interpreting the coefficients, Ca values cluster in the range 0.1–0.5 for all non-outlier cases. This implies that a finite contraction (effective discharge coefficient below unity) is required to reproduce the momentum flux consistent with measured penetration, i.e., Ca compensates for near-nozzle hole losses and unresolved cavitation/velocity-profile effects. β settles at moderate-to-high levels to maintain core coherence and peak fraction without excessive over-penetration, whereas α remains a secondary shaper of radial profiles. Case C remains the lone outlier. Because its low-load dynamics cannot be reconciled within the present ROSM assumptions without degrading other cases, we exclude Case C from the calibration dataset and focus the global calibration on the remaining operating points.

3.5. Validation results

We validated the globally calibrated ROSM on unseen operating points, assessing whether its accuracy matches that of the calibration set. Calibration uses cases A–F, with Case C excluded as an outlier. Validation uses cases G–I. In Fig. 11, the globally calibrated ROSM is analyzed for three new cases (G, H, and I) that were not part of the calibration set. The resulting penetration curves exhibit accuracy levels similar to those of the calibration cases, and the HRF distribution generally follows the CFD trends, with some overestimation of the peak value. In Cases G, H, and I, the globally tuned spray model ($\alpha = 1.93$, $\beta = 0.81$, $Ca = 0.21$) is validated by comparing its predicted penetration lengths and high-reactivity fuel (HRF) distributions against CFD results. The left-hand plots show that the model's penetration trajectories closely match the CFD curves in all three cases, although there are some minor deviations, such as a mild underprediction after the initial transient following start of injection. The right-hand plots illustrate the spatial HRF distribution, showing fuel fraction across zones, reflecting mixture stratification. The model captures the overall trend but

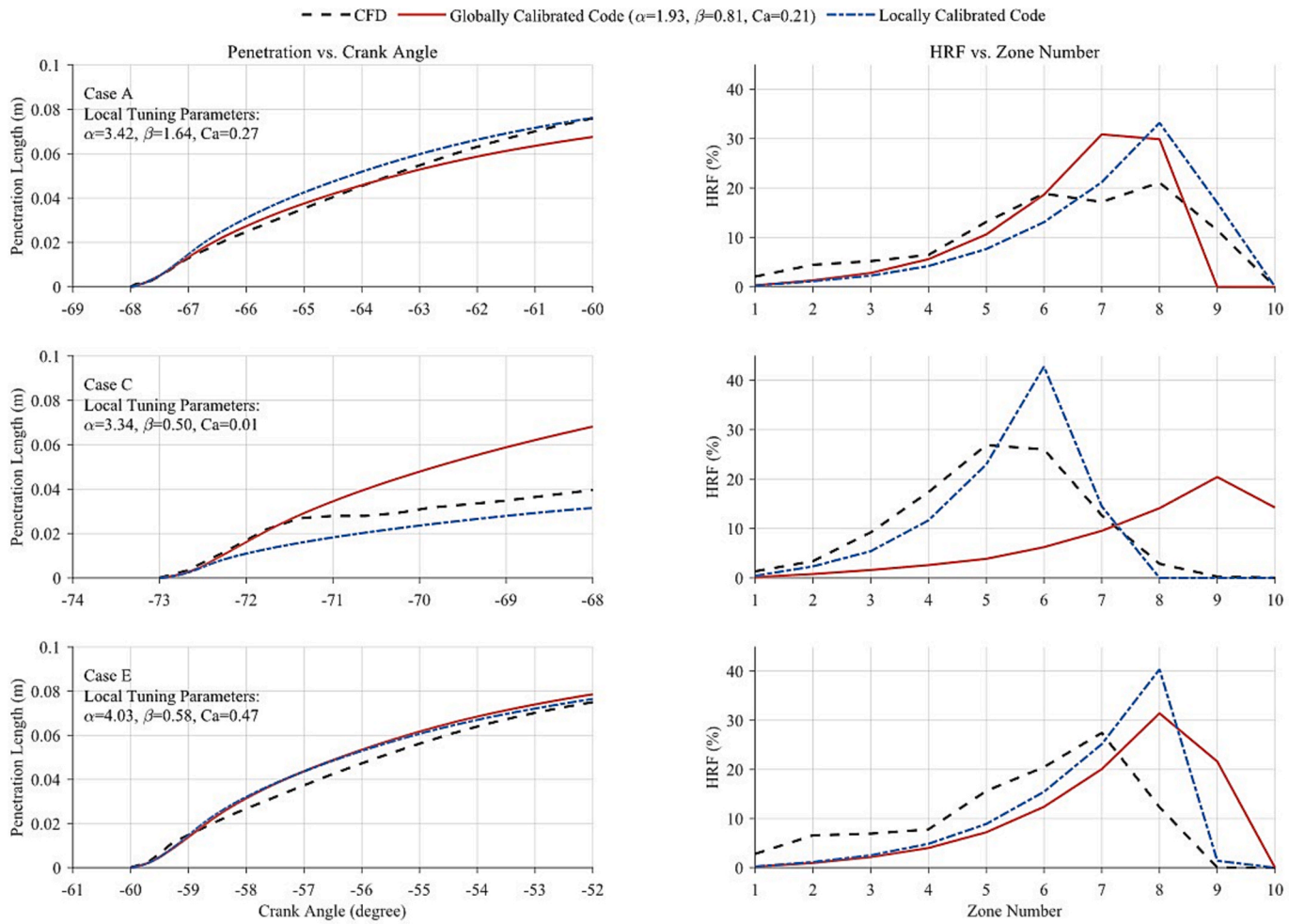

Fig. 10. Comparing CFD data with local and global tuning measures in penetration length (left) and HRF (right) for Cases A, C, and E: legends report the corresponding calibration coefficients.

overestimates the peak fuel concentration compared to CFD, especially in Cases I. Differences among these cases reflect variations in spray momentum and mixing. For instance, a higher injection momentum in Case I yields a longer penetration and a broader fuel plume (more dispersed stratification). The globally tuned model slightly over-predicts, shifting the peak fuel zone further downstream than in the CFD. However, the zone–wise HRF shares across zones 6–8 in Case I differ by less than ~ 1.5 percentage points, so a CFD maximum at zone 8 is effectively equivalent to a peak at zone 6 within the resolution of the mapping, and does not indicate a materially different stratification pattern. In contrast, Case G (with lower momentum or shorter injection) shows near-perfect agreement, with zero zone offset for the peak fuel zone. Case H falls in between, with intermediate penetration and a small shift in the peak of just one zone. These deviations arise because a fixed global calibration cannot perfectly capture each condition's ideal entrainment and evaporation rates, causing modest over- or under-penetration in different scenarios. Taken together, these qualitative comparisons are promising. The globally calibrated model reproduces the temporal evolution of penetration and the zonal stratification trend across G–I with consistent phasing and reasonable peak placement. To evaluate performance rigorously, we next quantified accuracy using the study's error metrics for peak fuel zone offset, penetration parity, and HRF parity. Figs. 12, 13, and 14 depict these accuracy results.

Fig. 12 summarizes how well the locally and globally calibrated models predict the zone number of the peak fuel distribution compared to CFD results the reported calibration and validation cases. The y-axis represents the difference in zone numbers (Code – CFD), while the x-axis shows the case identifiers. The dashed lines at ± 2 indicate the acceptable deviation threshold. All cases fall within this threshold, confirming that both calibrations reasonably capture the location of the peak fuel distribution. Local calibration achieves slightly better accuracy (e.g., two instances of zero-shift) but global calibration remains broadly usable and still meets the ± 2 requirement. The two largest offsets (+2 zones) occur in Cases F and I. These cases inject earliest (78° and 84° bTDC) and therefore at the lowest ambient densities and temperatures in the set (Table 6). Low ρ_a increases the jet momentum ratio ($\propto 1/\rho_a$), so the globally calibrated phenomenological model, which is tuned around denser conditions, advects the rich core too far before it entrains and spreads. As a result, it overestimates axial reach in this regime and places the peak fuel zone downstream of CFD by about two zones. In short, under low-density, early-injection conditions, the model over-weights momentum-controlled transport relative to entrainment during compression, producing a systematic downstream bias.

The parity plots in Fig. 13 and Fig. 14 compare the phenomenological model's predictions with CFD results for penetration length and HRF in all cases. The black parity line represents an ideal 1:1 agreement between the two models, while the dashed lines indicate the acceptable error margins.

In Fig. 13's plot of penetration length, the x-axis indicates the CFD penetration values and the y-axis represents the corresponding predictions from the phenomenological model for the same crank angle. Most data points cluster around the parity line, indicating a good agreement between the model and CFD. Some cases deviate slightly from the parity line but remain within the 14% error margin, suggesting

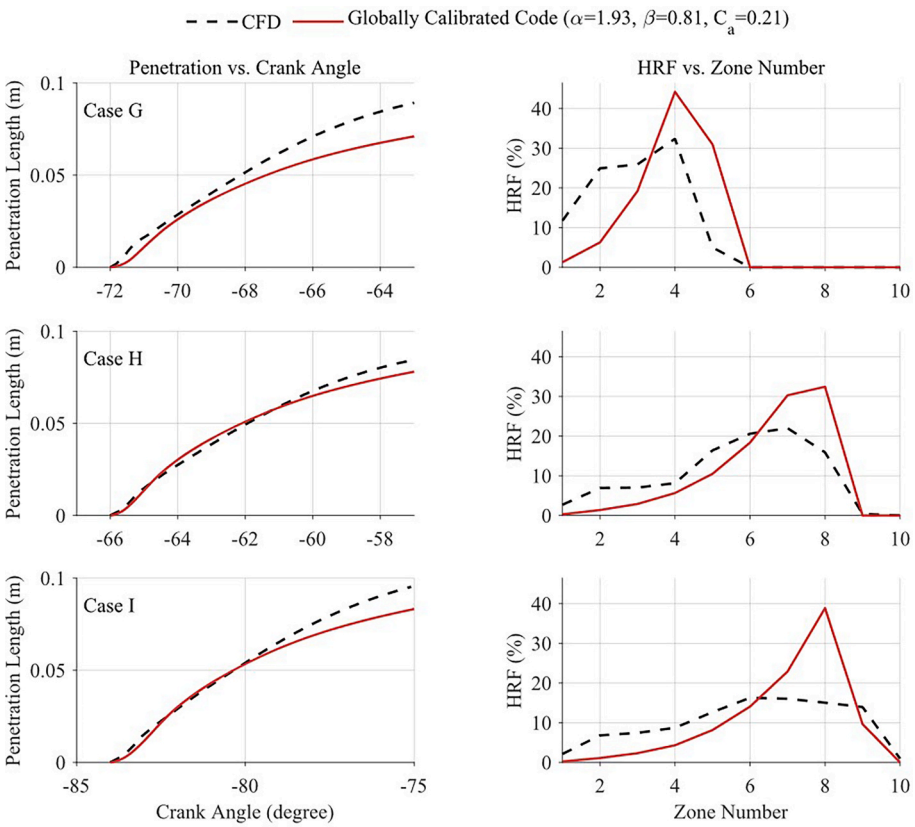

Fig. 11. Validation against CFD for cases G to I. Left column: spray tip penetration versus crank angle. Right column: zonal HRF distribution.

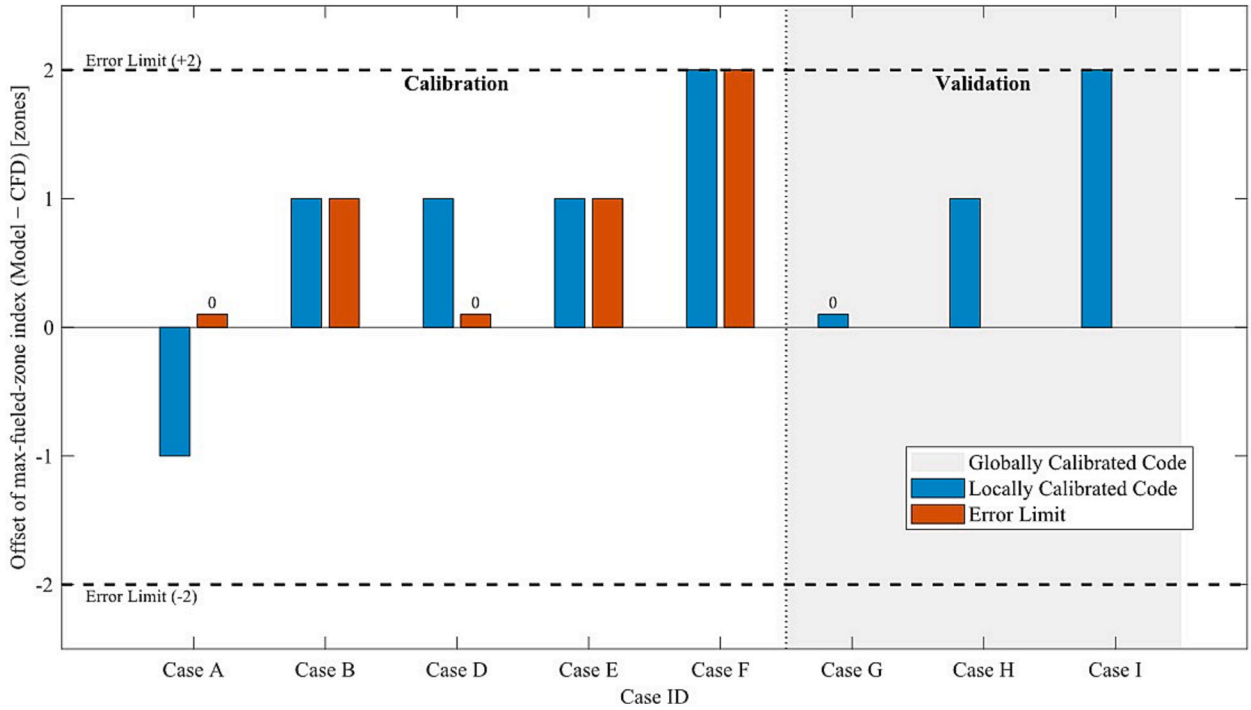

Fig. 12. Offset of the index of the peak fueled zone between model and CFD across calibration cases A to F (C excluded) and validation cases G to I.

that the model captures penetration length with reasonable accuracy. Also, the experimental data showed a nozzle hole-to-nozzle hole variation of approximately –23% to + 23% relative to the average penetration, meaning some sprays were up to 18% shorter or longer than the mean. Consequently, the 14% deviation observed in the CFD predictions lies well within the range of experimental scatter and is therefore acceptable considering the inherent variability of the injection system.

Fig. 14 compares HRF values predicted by the phenomenological

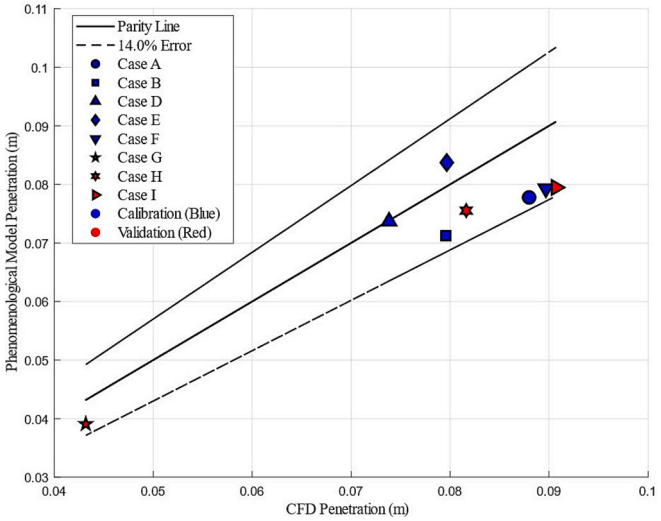

Fig. 13. Penetration parity of the globally calibrated ROSM versus CFD at the evaluation instant.

model and CFD. The x-axis represents CFD max HRF values, and the y-axis represents the model's HRF predictions for the same zone. The spread of data points is wider than the penetration length plot, implying a greater variation in prediction accuracy. Several cases deviate significantly from the parity line, but all fall inside the 40% error margin, suggesting that the phenomenological model can still predict HRF values reliably, albeit with a higher error range than penetration predictions. Cases such as A and H display a higher degree of overprediction, whereas most other scenarios fall within a more favorable error range. These results indicate that while the phenomenological model reliably captures penetration length, its HRF predictions can exhibit greater variability; however, for subsequent multi-zone combustion simulations, this larger peak-amplitude error is expected to be less critical than an error in peak location, because it mainly perturbs the local mixture-strength level, whereas the spatial placement of the maximum more directly governs ignition-kernel formation and the resulting heat-release phasing.

Taken together, Figs. 13 and 14 indicate that the globally calibrated ROSM attains robust predictive fidelity across unseen conditions. Penetration magnitudes remain within ~ 14% of CFD. The dispersion observed for peak HRF is larger, but consistent with reported inter–model/experiment spreads for diesel–spray stratification. Importantly, the validation cases exhibit error levels comparable to those of the calibration set, indicating no loss of generalization. Further refinements, such as evaporation/breakup sub–models, could narrow the HRF spread, but the present framework provides a reliable, injector–specific surrogate suitable for zonal mapping and subsequent ROSM analyses under the tested conditions.

4. Conclusion and outlook

This study developed a spray model for RCCI engine simulations and enhanced its ability to predict penetration length and HRF stratification. The model is valid for free sprays (pre-impingement) and pre-combustion mixing. Further work is needed to extend it to wall-impingement scenarios. A validated CFD model, itself corroborated by experimental data from a Wärtsilä 6L20 engine, was used to calibrate the spray model across a range of operating parameters. The key findings from this work are summarized below.

4.1. Key findings

- Across calibration and validation cases, spray-tip penetration from the globally calibrated ROSM agrees with CFD within 14%, preserving the temporal evolution and phasing over the free-field window.
- Peak HRF location is captured within ± 2 zones for all reported cases, whereas peak magnitude shows larger variance (occasionally up to ~ 40%). This pattern of good location fidelity with higher amplitude scatter is consistent with momentum-controlled jets where local entrainment and vaporization details act as second-order amplitude modifiers.
- The angled non-uniform CV-to-zone mapping constituted the main methodological advance of the present RCCI framework. Quantitatively, across the three representative mapping cases (A–C), it reduced the cumulative absolute error in peak-fuel-zone location from 5 and 6 zones for Methods 1 and 2 to 2 zones. Thus, the adopted

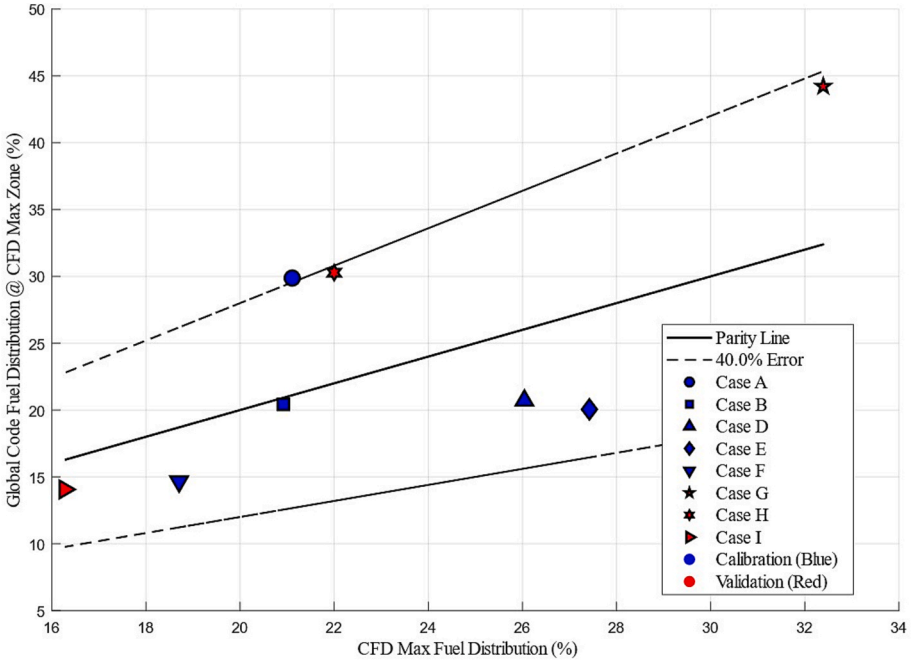

Fig. 14. Peak HRF parity of the globally calibrated ROSM versus CFD.

mapping lowered peak-location error by about 60–67% relative to the simpler alternatives, while preserving the physically more relevant placement of the rich core, despite some remaining over-prediction of peak magnitude.

- For reduced-order RCCI multi-zone combustion modeling, spray-induced fuel stratification can be supplied empirically, from CFD-derived maps, or from a predictive spray model. For one operating point, generating the CFD-based non-reactive spray/stratification reference used in this work required approximately 1088 s wall-clock time on 256 CPUs, whereas the corresponding ROSM prediction required approximately 1 s on a single CPU. Thus, compared with CFD-map-based spray-model preparation, which requires multiple CFD simulations to cover the target operating space, the present ROSM can substantially reduce the computational effort required to generate spray/stratification inputs.
- Ca (effective discharge/contraction) and β (exit-profile/momentum-flux shaping) are the dominant levers for penetration and stratification, whereas α chiefly fine-tunes radial profile shape, with minor impact on axial development. Peak-zone predictions are insensitive to zonal resolution, confirming robustness of the mapping.
- Local calibration yields the lowest case-specific errors, but a single global parameter set delivers calibration-level performance on unseen cases (G–I), maintaining the penetration and peak-zone accuracy noted above. The lowest load (density) case (C) behaved as an outlier: reducing penetration error forced misalignment in stratification metrics, so it was excluded from the final calibration domain.
- Validation cases exhibit error levels comparable to the calibration set, indicating no loss of fidelity when applying the globally tuned parameters to previously unseen operating conditions.

4.2. Outlook

The spray modeling approach developed in this study was intended for integration with the UVATZ model to enable rapid prototyping of advanced marine engines. Although the model has demonstrated promising capability, several extensions are required to improve its predictive robustness and application range. Future work is divided into two main pathways:

- **Near-term model-development** priorities include incorporation of wall-interaction effects, improved treatment of in-cylinder flow interaction, and development of a dedicated low-load extension. The present model has been validated only up to conditions before spray–wall interaction, whereas in RCCI operation the spray typically reaches the chamber walls before the start of combustion. Including wall impingement is therefore necessary to extend model validity toward combustion-relevant conditions. In addition, the current framework does not explicitly resolve the influence of in-cylinder cross-flow perpendicular to the spray axis, which should be addressed in broader engine-relevant validation. The behavior observed in Case C also indicates that low-load operation involves physical mechanisms not adequately represented by the current framework, especially in penetration and HRF prediction, motivating a dedicated low-load treatment.
- Higher-level application-oriented developments focus on coupling the ROSM with UVATZ/MZM-based reduced-order combustion models. Replacing fixed empirical or CFD-derived fuel-distribution inputs with dynamically predicted spray-driven distributions would improve combustion-model accuracy over a broader range of operating conditions and reduce the need for repeated CFD-based fuel-distribution mapping during model preparation. In such a framework, and after dedicated coupled-model validation, predictive cycle-resolved RCCI simulations are expected to be achievable with accuracy approaching that of fully reactive CFD, while reducing computational time to the order of minutes per cycle on a single CPU, compared with computational times on the order of days or weeks for fully reactive CFD simulations on high-performance computing clusters.

CRediT authorship contribution statement

Shadab Heidarabadi: Writing – review & editing, Writing – original draft, Visualization, Validation, Software, Methodology, Investigation, Funding acquisition, Formal analysis, Conceptualization. **Hamidreza Maleki Almani:** Writing – review & editing, Formal analysis. **Alireza Kakoee:** Writing – review & editing, Software, Resources. **Amin Andwari:** Writing – review & editing, Supervision. **Jari Hyvönen:** Writing – review & editing, Supervision, Resources, Conceptualization. **Maciej Mikulski:** Writing – review & editing, Supervision, Project administration, Methodology, Funding acquisition, Conceptualization.

Declaration of competing interest

The authors declare that they have no known competing financial interests or personal relationships that could have appeared to influence the work reported in this paper.

Acknowledgements

The work was conducted in the framework of the Computationally Aided Systems Engineering for Marine Advanced Technology for The Environment (CASEMATE) with financial support from Business Finland (ref. 2919/31/2022). The authors also acknowledge the research grant from the Fortum and Neste Foundation grant no. 20250019. The authors also thank Mr. David Wilcox for proofreading the manuscript and providing helpful stylistic suggestions.

Appendix A. Supplementary data

The supplementary material includes five supporting files related to the reduced-order spray model and CFD-based validation workflow: CFD-to-zonal fuel-distribution post-processing workflow; ROSM time-marching and zonal mapping workflow; local/global ROSM calibration workflow; CFD sub-model rationale table; and CFD contour sequence showing n-dodecane mass-fraction evolution for Case A from SOI to SOC.

Supplementary data to this article can be found online at https://doi.org/10.1016/j.fuel.2026.140328.

Data availability

The data that has been used is confidential.

References

[1] Ali I. The world's maritime industry in the 21st century: challenges, expectations, and directions. South East Asian Marine Sci. J. 2025;2:64–75. https://doi.org/10.61761/seamas.2.2.64-75.
[2] Deng S, Mi Z. A review on carbon emissions of global shipping. Marine Dev. 2023;1. https://doi.org/10.1007/s44312-023-00001-2.
[3] International Maritime Organization (IMO), "Resolution MEPC.377(80) (adopted on 7 July 2023): 2023 IMO Strategy on Reduction of GHG Emissions from Ships," MEPC 80/17/Add.1, Annex 15, 7 July 2023. Accessed: 4 Apr. 2026. Available: https://wwwcdn.imo.org/localresources/en/OurWork/Environment/Documents/annex/MEPC%2080/Annex%2015.pdf.
[4] Aakko-Saksa PT, Lehtoranta K, Kuittinen N, Järvinen A, Jalkanen J-P, Johnson K, et al. Reduction in greenhouse gas and other emissions from ship engines: current trends and future options. Prog Energy Combust Sci 2023;94:101055. https://doi.org/10.1016/j.pecs.2022.101055.
[5] Harris S, Weinzettel J, Bigano A, Källmén A. Low carbon cities in 2050? GHG emissions of European cities using production-based and consumption-based emission accounting methods. J Clean Prod 2020;248:119206. https://doi.org/10.1016/j.jclepro.2019.119206.
[6] Estevez R, Aguado-Deblas L, López-Tenllado FJ, Bautista FM, Romero AA, Luna D. Internal combustion engines and carbon-neutral fuels: a perspective on emission neutrality in the European Union. Energies (Basel) 2024;17. https://doi.org/10.3390/en17051172.

[7] García A, Monsalve-Serrano J, Guzmán-Mendoza MG, Iñiguez E. Technical evaluation of low-carbon fuels as a decarbonization pathway of the light-duty transport sector. Fuel 2024;369:131772. https://doi.org/10.1016/j.fuel.2024.131772.

[8] Modabberian A, Storm X, Shamekhi A-M, Vasudev A, Zenger K, Hyvönen J, et al. Low temperature combustion modeling and predictive control of marine engines. Appl Sci 2024;14. https://doi.org/10.3390/app14052033.

[9] Kakoee A, Mikulski M, Vasudev A, Axelsson M, Hyvönen J, Salahi MM, et al. Start of injection influence on in-cylinder fuel distribution, engine performance and emission characteristic in a RCCI marine engine. Energies (Basel) 2024;17. https://doi.org/10.3390/en17102370.

[10] Vasudev A, Kakoee A, Axelsson M, Almani HM, Hyvönen J, Mikulski M. Advancing autonomy of chemical kinetics based multizone models for reactivity controlled compression ignition engines. Energy Convers Manag 2024;312:118562. https://doi.org/10.1016/j.enconman.2024.118562.

[11] Saana H, Maciej M, Emma S, Xiaoguo S, Seppo N. Toward a digital twin of a mid-speed marine engine: from detailed 1D engine model to real-time implementation on a target platform. Int J Engine Res 2023;24:4553–71. https://doi.org/10.1177/14680874221106168.

[12] Kakoee A, Hunicz J, Mikulski M. Integrated 1D simulation of aftertreatment system and chemistry-based multizone RCCI combustion for optimal performance with methane oxidation catalyst. J Mar Sci Eng 2024;12. https://doi.org/10.3390/jmse12040594.

[13] Vasudev A, Soleimani A, Hyvönen J, Mikulski M. Feasible route towards decarbonising marine transport with flexible, hydrogen – enriched, reactivity controlled compression ignition mid-speed engines. Int J Hydrogen Energy 2025;142:1196–210. https://doi.org/10.1016/j.ijhydene.2025.02.152.

[14] Mikulski M, Ovaska T, Rabetino R, Kangasjärvi M, Myllykangas A. Clean propulsion technologies: securing technological dominance for the Finnish marine and off-road powertrain sectors. Energies (Basel) 2025;18:1240. https://doi.org/10.3390/en18051240.

[15] Dwarshala SKR, Rajakumar SS, Kummitha OR, Venkatesan EP, Veza I, Samuel OD. A review on recent developments of RCCI engines operated with alternative fuels. Energies (Basel) 2023;16. https://doi.org/10.3390/en16073192.

[16] Heidarabadi S, Khoshbakhti Saray R, Neshat E. Detailed kinetic study on methane/diesel RCCI combustion. Int J Engine Res 2021;22:2422–41. https://doi.org/10.1177/1468087420954012.

[17] Li Y, Jia M, Xu L, Bai XS. Multiple-objective optimization of methanol/diesel dual-fuel engine at low loads: a comparison of reactivity controlled compression ignition (RCCI) and direct dual fuel stratification (DDFS) strategies. Fuel 2020;262. https://doi.org/10.1016/j.fuel.2019.116673.

[18] Guo X, Luo H, Liu L, Liu K, Ge J, Nishida K. Towards green marine engines: a review of methanol fueled internal combustion engine. Green Energy Resour 2026;4:100168. https://doi.org/10.1016/j.gerr.2026.100168.

[19] Poorghasemi K, Saray R, Solmaz H, Mousavi S, Zehni A. Multi-dimensional 3D-CFD/chemical-kinetics modeling of natural gas–diesel RCCI engines: combustion phasing, efficiency and emissions. Eng. Perspect. 2026;6:69–82. https://doi.org/10.64808/engineeringperspective.1802746.

[20] Ren Z, Lin C, Haiqiao W, Jinguang Li, Yi D, Rui C, et al. Experimental investigation on reactivity-controlled compression ignition (RCCI) combustion characteristic of n-heptane/ammonia based on an optical engine. Int J Engine Res 2023;24:2478–88. https://doi.org/10.1177/14680874221124452.

[21] Fakhari A, Gharehghani A, Salahi MM, Andwari A. RCCI combustion of ammonia in dual fuel engine with early injection of diesel fuel. Fuel 2024;365. https://doi.org/10.1016/j.fuel.2024.131182.

[22] Fakhari AH, Gharehghani A, Salahi MM, Andwari AM. Numerical investigation of the hydrogen-enriched ammonia-diesel RCCI combustion engine. Fuel 2024;375:132579. https://doi.org/10.1016/j.fuel.2024.132579.

[23] Elkelawy M, El Shenawy EA, Mohamed SA, Elarabi MM, Alm-Eldin BH. Impacts of EGR on RCCI engines management: a comprehensive review. Energy Convers Manage: X 2022;14:100216. https://doi.org/10.1016/j.ecmx.2022.100216.

[24] Duan H, Jia M, Wang H, Li Y, Xia G. Control of low-temperature polyoxymethylene dimethyl ethers (PODEn)/gasoline combustion considering fuel concentration, fuel reactivity, and intake temperature at low loads. Fuel 2023. https://doi.org/10.1016/j.fuel.2022.126823.

[25] Ling Su, Zhou L, Liu S, Zhong H. Decreasing hydrocarbon and carbon monoxide emissions of a natural-gas engine operating in the quasi-homogeneous charge compression ignition mode at low loads. Proc. Inst. Mech. Eng., Part D: J. Autom. Eng. 2005;219:1125–31. https://doi.org/10.1243/095440705X34793.

[26] Kakoee A, Golbaghi K, Cafari A, Vasudev A, Mehranfar S, Andwari AM, et al. The interplay between combustion and component thermal loading in next-generation marine engines employing reactivity-controlled compression ignition. Energies (Basel) 2026;19. https://doi.org/10.3390/en19010083.

[27] Qin T, Zhang F, Li J, Liao B, Lin X, Guo Y, et al. Effect of knock on piston thermal load of a high compression ratio natural gas engine based on stepwise decoupling calculation. Appl Therm Eng 2024;255:123996. https://doi.org/10.1016/j.applthermaleng.2024.123996.

[28] Kim J, Soleimani A, Nousiainen P, Axelsson M, Mikulski M. Variable valve actuation (VVA) for next-generation marine and off-road engines: a comprehensive review for meeting future emissions legislation. Appl Energy 2026;403. https://doi.org/10.1016/j.apenergy.2025.127133.

[29] Soleimani A, Kim J, Axelsson M, Hyvonen J, Mikulski M. Exhaust thermal management in a dual-fuel marine engine via fully variable valve actuation and wastegate lambda control. 2025. https://doi.org/10.4271/2025-24-0085.

[30] Vasudev A, Cafari A, Axelsson M, Mikulski M, Hyvonen J. Towards next generation control-oriented thermo-kinetic model for reactivity controlled compression ignition marine engines. In: SAE Technical Papers. SAE International; 2022. https://doi.org/10.4271/2022-01-1033.

[31] Vasudev A, Mikulski M, Balakrishnan PR, Storm X, Hunicz J. Thermo-kinetic multi-zone modelling of low temperature combustion engines. Prog Energy Combust Sci 2022;91. https://doi.org/10.1016/j.pecs.2022.100998.

[32] De Bellis V, Malfi E, Lanotte A, Fasulo G, Bozza F, Cafari A, et al. Development of a phenomenological model for the description of RCCI combustion in a dual-fuel marine internal combustion engine. Appl Energy 2022;325. https://doi.org/10.1016/j.apenergy.2022.119919.

[33] De Bellis V, De Felice M, Malfi E, Bozza F, Cafari A, Cimarello A, et al. Development and validation of phenomenological models for combustion and emissions of a dual-fuel marine engine supplied with ammonia. Int J Hydrogen Energy 2025;170:151020. https://doi.org/10.1016/j.ijhydene.2025.151020.

[34] Liu L, Peng Y, Liu D, Han C, Zhao N, Ma X. A review of phenomenological spray penetration modeling for diesel engines with advanced injection strategy. Int J Spray Combust Dyn 2020;12. https://doi.org/10.1177/1756827720934067.

[35] Wakuri Y, Fujii M, Amitani T, Tsuneya R. Studies on the penetration of fuel spray in a diesel engine. JSME Int J Series B-Fluids Thermal Eng 1959;3:123–30.

[36] Hiroyasu H, Arai M. Structures of fuel sprays in diesel engines. In: International Congress & Exposition. SAE International; 1990. https://doi.org/10.4271/900475.

[37] Siebers DL. Recent developments on diesel fuel jets under quiescent conditions. In: Arcoumanis C, Kamimoto T, editors. Flow and Combustion in Reciprocating Engines. Berlin, Heidelberg: Springer Berlin Heidelberg; 2009. p. 257–308. . https://doi.org/10.1007/978-3-540-68901-0_5.

[38] Desantes J, Payri R, Salvador FJ, Gimeno J. Prediction of spray penetration by means of spray momentum flux. 2006. https://doi.org/10.4271/2006-01-1387.

[39] Kostas DJ, Honnery DR, Soria J. Time resolved measurements of the initial stages of fuel spray penetration. Fuel 2009;88:2225–37. https://doi.org/10.1016/j.fuel.2009.05.013.

[40] Zhou X, Li T, Yi P. Modeling of diesel spray tip penetration during start-of-injection transients. Int J Engine Res 2021;22:3013–29. https://doi.org/10.1177/1468087420957852.

[41] Zhai C, Chang F, Jin Y, Luo H. Investigations on the diesel spray characteristic and tip penetration model of multi-hole injector with micro-hole under ultra-high injection pressure. Sustainability 2023;15. https://doi.org/10.3390/su151411114.

[42] Zhai C, Zhang J, Li K, Dong P, Jin Y, Chang F, et al. Comparative analysis and normalization of single-hole vs. multi-hole spray characteristics: 1st report on spray characteristic comparison. Green Energy Resour 2025;3:100120. https://doi.org/10.1016/j.gerr.2025.100120.

[43] Kurapati V, Anders B, Seidel L, Mauss F. Fast CFD Diesel engine modelling using the 1-dimensional SprayLet approach. 2024. https://doi.org/10.4271/2024-01-2684.

[44] Pastor JV, Javier López J, García JM, Pastor JM. A 1D model for the description of mixing-controlled inert diesel sprays. Fuel 2008;87:2871–85. https://doi.org/10.1016/j.fuel.2008.04.017.

[45] Musculus MPB, Kattke K. Entrainment waves in diesel jets. SAE Int J Engines 2009;2(1):1170–93. https://doi.org/10.4271/2009-01-1355.

[46] Liu L, Mei Q, Jia W. A flexible diesel spray model for advanced injection strategy. Fuel 2021. https://doi.org/10.1016/j.fuel.2021.122784.

[47] Bao Z, Horibe N, Ishiyama T. A Study on Diesel Spray Characteristics for Small-Quantity Injection 2018. https://doi.org/10.4271/2018-01-0283.

[48] Kurapati V, Anders B, Seidel L, Mauss F. SprayLet: One-dimensional interactive cross-sectionally averaged spray model. 2023. https://doi.org/10.4271/2023-24-0083.

[49] De Felice M, De Bellis V, Malfi E, Gambardella A, Bozza F, Cafari A, et al. A novel phenomenological model for stratification-controlled low temperature combustion applied to a dual-fuel marine internal combustion engine supplied with natural gas and light fuel oil. Fuel 2025;386:134218. https://doi.org/10.1016/j.fuel.2024.134218.

[50] Mopuri L, Grahn V, Sedarsky D, Hyvönen J. Shape/penetration analysis and comparisons of isolated spray plumes in a multi-hole Diesel spray. Exp Fluids 2024;65:92. https://doi.org/10.1007/s00348-024-03829-6.

[51] Payri R, Gimeno J, Bardi M, Plazas AH. Study liquid length penetration results obtained with a direct acting piezo electric injector. Appl Energy 2013;106:152–62. https://doi.org/10.1016/j.apenergy.2013.01.027.

[52] Baert R, Frijters P, Somers LMT, Luijten C, Boer W. Design and operation of a high pressure, high temperature cell for HD diesel spray diagnostics: guidelines and results. SAE Technical Papers. 2009. 10.4271/2009-01-0649.

[53] Beale J, Reitz R. Modeling spray atomization with the Kelvin-Helmholtz/Rayleigh-Taylor hybrid model. Atom Sprays 1999;9:623–50. https://doi.org/10.1615/AtomizSpr.v9.i6.40.

[54] Froessling N. Evaporation, heat transfer, and velocity distribution in two-dimensional and rotationally symmetrical laminar boundary-layer flow. NACA Technical Memorandum 1432. Washington, DC: National Advisory Committee for Aeronautics; 1958.

[55] Schmidt DP, Rutland CJ. A new droplet collision algorithm. J Comput Phys 2000;164:62–80. https://doi.org/10.1006/jcph.2000.6568.

[56] Kim S, Lee DJ, Lee CS. Modeling of binary droplet collisions for application to inter-impingement sprays. Int J Multiph Flow 2009;35:533–49. https://doi.org/10.1016/j.ijmultiphaseflow.2009.02.010.

[57] Kobashi Y, Zama Y, Kuboyama T. Modeling wall film formation and vaporization of a gasoline surrogate fuel. Int J Heat Mass Transf 2020;147:119035. https://doi.org/10.1016/j.ijheatmasstransfer.2019.119035.

[58] Wang J, Hu X. Application of RNG k-ε turbulence model on numerical simulation in vehicle external flow field. Appl Mech Mater 2012;170–173:3324–8. https://doi.org/10.4028/www.scientific.net/AMM.170-173.3324.

[59] Raju M, Dahale A, Ge X. Improving residual convergence of steady-state non-reacting and reacting spray simulations. 2023. LASS-Americas 32nd Annual Conference on Liquid Atomization and Spray Systems. 2022.
[60] Yao T, Pei Y, Zhong B-J, Som S, Lu T, Luo KH. A compact skeletal mechanism for n-dodecane with optimized semi-global low-temperature chemistry for diesel engine simulations. Fuel 2017;191:339–49.
[61] Varatharajan K, Cheralathan M. Influence of fuel properties and composition on NOx emissions from biodiesel powered diesel engines: a review. Renew Sustain Energy Rev 2012;16:3702–10. https://doi.org/10.1016/j.rser.2012.03.056.
[62] Cant RS, Ahmed U, Fang J, Chakarborty N, Nivarti G, Moulinec C, et al. An unstructured adaptive mesh refinement approach for computational fluid dynamics of reacting flows. J Comput Phys 2022;468:111480. https://doi.org/10.1016/j.jcp.2022.111480.
[63] Gnedin NY, Semenov VA, Kravtsov AV. Enforcing the Courant–Friedrichs–Lewy condition in explicitly conservative local time stepping schemes. J Comput Phys 2018;359:93–105. https://doi.org/10.1016/j.jcp.2018.01.008.
[64] Ruth D, O'Connor J. Development and verification of reduced-order model for diesel spray penetration and spreading during wall impingement. SAE Technical Papers. SAE International; 2017. 10.4271/2017-01-0814.
[65] Washburn EW. The dynamics of capillary flow. Phys Rev 1921;17:273–83. https://doi.org/10.1103/PhysRev.17.273.
[66] Zayed M. Lecture notes (Flow through Orifices). 2020. https://doi.org/10.13140/RG.2.2.32468.96648.
[67] Wärtsilä Finland Oy, Product Guide: Wärtsilä 20DF, Issue 1/2025 (26 Feb. 2025), Wärtsilä Marine Business, Vaasa, Finland, 2025 (PDF).
[68] Shields MD, Zhang J. The generalization of Latin hypercube sampling. Reliab Eng Syst Saf 2016;148:96–108. https://doi.org/10.1016/j.ress.2015.12.002.
[69] Zhou X, Li T, Wei Y, Wang N. Scaling liquid penetration in evaporating sprays for different size diesel engines. Int J Engine Res 2020;21:1662–77. https://doi.org/10.1177/1468087419889835.
[70] Ailaboina A, Saha K. On modeling of spray G ECN using ROI-based Eulerian-Lagrangian simulation. Front Mech Eng 2022;8. https://doi.org/10.3389/fmech.2022.880635.
[71] Kakoee A, Vasudev A, Smulter B, Hyvonen J, Mikulski M. A predictive 1D modeling framework for reactivity-controlled compression ignition engines, via a chemistry-based, multizone combustion object. SAE Technical Papers. SAE International; 2023. 10.4271/2023-24-0001.
[72] Naber JD, Siebers DL. Effects of gas density and vaporization on penetration and dispersion of diesel sprays. SAE Trans 1996;105:82–111. https://doi.org/10.4271/960034.